

Two-dimensional spectral simulations of neutron star spreading layers

Pavel Abolmasov^{1,2}, Joonas Nättilä³, and Juri Poutanen^{1,3,4}

¹ Department of Physics and Astronomy, FI-20014 University of Turku, Finland e-mail: pavel.abolmasov@gmail.com

² Sternberg Astronomical Institute, Moscow State University Universitetsky pr., 13, Moscow 119234

³ Nordita, KTH Royal Institute of Technology and Stockholm University,

⁴ Space Research Institute of the Russian Academy of Sciences, Profsoyuznaya str. 84/32, 117997 Moscow, Russia

Received ; accepted

ABSTRACT

Context. Accretion boundary layer (BL) is an important constituent of the dynamics of accretion onto weakly magnetized objects including neutron stars in low-mass X-ray binaries and non-magnetic white dwarfs. As the angular momentum transfer between the accreting material and the star is inefficient, much of the kinetic energy of the flow is dissipated in the spreading layer (SL). In contrast with the classical approach to a BL as some part of the disc strongly deviating from Keplerian rotation, SL is viewed as a two-dimensional structure on the surface of the star, pushed away from the equatorial plane of the disc by pressure gradients.

Aims. We consider the internal dynamics of an SL in order to trace the re-distribution of the angular momentum and to study the variability patterns emerging in the flow. These are interesting to compare to the observed variability of low-mass X-ray binaries.

Methods. We derive the system of equations describing the two-dimensional radiative hydrodynamics on a sphere and including a number of relevant source and sink terms. To solve the system, we use a spectral method involving decomposition into spherical harmonics. The method is realized in the form of a free open-source code *SLayer*. We consider the case of an SL rotating at approximately the local Keplerian velocity interacting with a pre-existing matter initially co-rotating with the star.

Results. We find that, during accretion, at least two different instabilities come into play. The first one is a heating instability capable of moving large portions of cool, rapidly rotating material from the layer to higher latitudes, simultaneously breaking the axial symmetry of the flow. The second one is the shear instability, working on smaller scales near the discontinuities in rotation velocity. Development of these instabilities leads to angular momentum exchange between the newly accreted, rapidly rotating material of the layer and the slowly rotating pre-existing matter. We compute artificial light curves for a SL viewed at different inclination angles. Most of the simulated light curves show oscillations at frequencies close to 1 kHz. Oscillations observed in our simulations are most likely inertial modes excited by shear instabilities near the boundary of the SL. Their frequencies, dependence on flux, and amplitude variations closely resemble those of the high-frequency pair quasi-periodic oscillations (QPOs) observed in many low-mass X-ray binaries.

Conclusions. We find that, though inefficient at angular momentum transfer, shear instabilities can excite local r-modes at high latitudes. The observational properties of these modes are very much similar to the properties of high-frequency QPOs in low-mass X-ray binaries.

Key words. accretion, accretion discs – methods: numerical – stars: neutron

1. Introduction

For a non-magnetized accretor with a surface, fluid or solid, non-relativistic disc accretion releases only about half of the gravitational binding energy. The other half is stored as kinetic energy of the flow (see for instance Sibgatullin & Sunyaev 2000). As the accretor is unlikely to rotate close to its Roche limit, larger part of this energy will still dissipate close to the surface of the accretor, in what is called boundary layer (BL). There is no commonly accepted view of a BL, even its basic geometry is uncertain.

Boundary layers are expected to appear during disc accretion onto stars and compact objects with relatively weak magnetic fields, incapable of creating a magnetosphere. For neutron stars (NS), this happens for a surface magnetic field $B \lesssim 10^8$ G, if the accretion rate is about Eddington. Lower mass accretion rate sets a stronger limit for the magnetic field, proportional to the square root of the accretion rate. This case is relevant for old NSs in low-mass X-ray binaries (LMXBs). In particular, BL apparently plays an important role in the so-called Z and atoll sources (as classified by Hasinger & van der Klis 1989). Com-

bined spectral and timing observations of LXMB allow to separate the contribution of the BL from that of the accretion disc (Gilfanov et al. 2003; Revnivtsev & Gilfanov 2006). Emission of the boundary layer is hotter, having a colour temperature of about $T_e \approx 2.5$ keV. The BL spectral component is more variable than the disc on the short, dynamical, timescales. In particular, the highest-frequency, kilohertz, quasi-periodic oscillations (kHz QPO; see for instance van der Klis 2000) can be interpreted as some type of BL activity. This is supported by the fact that, while the properties of all the low-frequency QPO types are quite similar in NS and black-hole LMXBs, kHz QPO behave in a profoundly different way for NS sources (Motta et al. 2017). This difference is natural to attribute to existence of a solid surface and a BL.

These QPOs are often observed in pairs, with the distance between the peaks close to the frequency of burst oscillations that is itself considered equal or close either to the spin frequency of the NS (van der Klis 2000), or to one half of it (Méndez et al. 1998; Wijnands et al. 2003). As the observational data accumulate, the picture gets more complicated, favouring rather a uni-

versal, sometimes variable, frequency difference of $\Delta f \sim 300\text{Hz}$ (Méndez & Belloni 2007), close to but not equal or proportional to the spin frequency. Normally, there are only two kHz peaks present. One explanation is a bright spot rotating at a frequency of the order of Keplerian frequency (for a conventional NS with a mass of $1.5 M_{\odot}$, and radius 12 km, linear Keplerian frequency is $f_K \approx 1.5 \text{ kHz}$) and producing one peak due to visibility effects and the other due to interaction with non-axisymmetric structures at the surface of the NS. This interpretation is known as a beat-frequency model (first apparently proposed by Lamb et al. 1985 in the context of a different QPO type) and implies strict equality between the difference in the frequencies of the two QPOs and the spin frequency of the NS. Also, different types of beat-frequency models, not involving a BL, were proposed to explain the properties of kHz QPOs. Best known are the magnetospheric beat-frequency model (Psaltis et al. 1998), considering LMXBs as magnetized accretors with very compact magnetospheres, and the sonic-point beat frequency model (Miller et al. 1998). The latter relies on the strong gravity effects that place, for a conventional NS, the last stable Keplerian orbit at a radius somewhat larger than the radius of the star. Both models require some mechanism generating a narrow-band variability at the local Keplerian frequency. Resonances between Keplerian, epicyclic, and vertical epicyclic frequencies emerging in general relativistic solutions are apparently a good explanation for the kHz QPOs in black hole systems (Kluźniak & Abramowicz 2001; Kluźniak et al. 2004), but predict a fixed ratio 2:3 for the peak frequencies. In NS systems, the frequency ratio varies in rather broad limits, and 2:3 is only a crude approximation. The caveats in the conventional resonance model were considered by Rebusco (2008).

QPO frequencies shift with time, remaining correlated with the observed flux on short timescales (hours and less) and uncorrelated on longer time spans. This creates parallel tracks in the flux vs QPO-frequency plot (Méndez et al. 1999; van der Klis 2001) and suggests that a BL possesses a characteristic correlation timescale much longer than even the viscous timescales in the disc (on which the mass accretion rate varies). It is difficult to suggest a way an accretion disc may produce the parallel tracks, as the variability of the accretion disc is governed essentially by a single parameter, the mass accretion rate. If the BL is weakly coupled with the surface of the star, it is a good candidate to such an “integrator”. Rich phenomenology of kHz QPOs is a potentially important source of information about the NS itself and the physics of the flows close to its surface. However, besides the numerous observational clues and the variety of existing models, there is no understanding of the mechanisms and exact relations between the quantities.

Classical approach to BL considers the flow as some part of the disc (Pringle 1977; Popham & Narayan 1995) where rotation velocity deviates strongly from Keplerian rotation and matches the rotation rate of the star at the inner edge. Strongly non-Keplerian rotation means that the approximations used as the base for the thin disc approach are no more valid, and the radial structure of the flow is strongly affected by radial pressure gradient. Another problem is the efficiency of angular momentum exchange in the BL. In a hot (ionized) accretion disc with a rotation law close to Keplerian, there is an outward angular momentum transfer provided by the magnetohydrodynamic (MHD) turbulence generated by magneto-rotational instability (or MRI, introduced to the astrophysical context by Balbus & Hawley 1991), operational when and only when the angular velocity decreases with the cylindrical radial coordinate. For a BL, the rotation profile does not in general fulfil the necessary condition for MRI.

It is unclear which physical mechanisms are actually responsible for the angular momentum exchange between the accreted matter and the surface of the star. In practically any possible BL model, Rayleigh stability criterion (Rincon et al. 2007) is satisfied. Hydrodynamic turbulence is still produced for large enough Reynolds numbers (see Zhuravlev & Razdoburdin 2018 for a detailed analysis), but the amplitudes of turbulent motions are apparently insufficient for efficient angular momentum transfer. The very existence of an extremely long correlation timescale mentioned above suggests that, whatever is the mechanism of angular momentum transfer, it is extremely slow and inefficient.

A good candidate for such a mechanism is supersonic shear instability at the interface between the star and the BL (Belyaev & Rafikov 2012; Belyaev et al. 2013; Philippov et al. 2016; Belyaev & Quataert 2018). Unlike the classical, sub-sonic Kelvin-Helmholtz instability, oblique waves rather than vortices are generated. Moving in a shear velocity flow, the waves create Reynolds stress and thus provide effective non-local viscosity not only in the BL but also in the accretion disc. The numerical studies mentioned above considered a two-dimensional problem either in the equatorial plane or in the meridional plane that allowed to concentrate on the interaction between the star and the disc. All the simulations, however, agree on the inefficiency of angular momentum transfer provided by oblique waves and associated turbulence. At least, in the accretion disc, their contribution is negligible compared to conventional MRI-driven MHD turbulence.

If the angular momentum exchange between the accreting matter and the material of the star is inefficient, rapidly rotating matter would accumulate on the surface, pushed to higher latitudes by pressure gradient. The radial dimension of such a flow, as well as of a conventional BL, is second order in relative disc thickness, much smaller than its vertical (along the polar angle) extent (Papaloizou & Stanley 1986). Then, one can treat the flow as two-dimensional (2D) on the surface of the NS fed by matter and angular momentum injection from the disc. This approach known as *spreading layer* (SL) was introduced by Inogamov & Sunyaev (1999) and further developed in Suleimanov & Poutanen (2006) and Inogamov & Sunyaev (2010). For the case of accreting white dwarfs, this model was considered by Piro & Bildsten (2004b) and used to explain a certain type of QPOs observed in cataclysmic variables, the so-called dwarf-nova oscillations, DNO (Piro & Bildsten 2004a). The angular momentum transfer within the SL depends on the dynamics of the flow itself, existing oscillation and instability modes. It is quite probable that certain hydrodynamical phenomena will provide an efficient way to transfer momentum within the SL and thus define its internal dynamics. In this paper, we will try to answer this question using numerical hydrodynamical simulations.

2D hydrodynamics on a rotating sphere is an important subject in geophysics and astrophysics, as many roundly-shaped bodies including planets, stars, and NSs, have fluid atmospheres. Vertically integrated equations of hydrodynamics lead to the system of *shallow water* equations (see for instance Vreugdenhil 1990), normally used in geophysics for weather forecast in combination with spectral methods (Jakob-Chien et al. 1995). Spectral methods provide much higher accuracy than finite-difference methods on an equally fine grid, and are quite robust and stable for subsonic flows. Rotation in a SL is, however, practically always supersonic, that makes the flow compressible and its simulations potentially prone to numerical instabilities. This makes numerical simulations of spreading layers technically challenging. On the other hand, using spherical harmonics is natural in spherical coordinates and allows to avoid the singularity the

spherical grid has near its axis. We provide our full simulation code SLAYER as an open-source software¹.

The paper is organized as follows. In Sect. 2, we formulate the physical problem and derive all the basic equations. Results of the simulations are given in Sect. 3. Applications and limitations of the model are discussed in Sect. 4. We conclude in Sect. 5. Detailed description of the numerical techniques used and the tests and SL models is given in Appendix B.

2. Physical model

2.1. Scales and dimensionless quantities

Natural time scale in the vicinity of a relativistic object is

$$t_g = \frac{GM}{c^3} \simeq 6.9 \times 10^{-6} \text{ s}, \quad (1)$$

that is the approximate light-crossing or dynamical time scale at the event horizon. Corresponding radius is

$$R_g = \frac{GM}{c^2} \simeq 2 \frac{M}{1.4 M_\odot} \text{ km}. \quad (2)$$

Radius of the NS is taken as $R_* \simeq 12 \text{ km} \simeq 6R_g$ assuming a mass of $1.4 M_\odot$ (see for instance the estimates of masses and radii in Miller & Lamb 2016; Nättilä et al. 2017).

All the geometrical and kinematical quantities are naturally normalized by combinations of these spatial and temporal scales. In particular, velocities in the units of the speed of light c are used. There is no natural convenient scale for the surface mass density Σ , as the opacity does not play as fundamental a role as, for instance, in accretion discs, hence we use physical quantities (g cm^{-2}) for Σ and normalize internally the surface density by an arbitrary scale set either to 10^4 g cm^{-2} or to 10^8 g cm^{-2} for the simulations presented in this paper. Evidence for a very long correlation timescale t_{corr} suggests a characteristic value of

$$\Sigma_{\text{ch}} \sim \frac{\dot{M} t_{\text{corr}}}{4\pi R^2} \simeq 10^8 \frac{\dot{M}}{10^{17} \text{ g s}^{-1}} \frac{t_{\text{corr}}}{1 \text{ hour}} \left(\frac{12 \text{ km}}{R_*} \right)^2 \text{ g cm}^{-2}. \quad (3)$$

The physical meaning of this value is the mean surface density, while t_{corr} is a characteristic time of mass depletion/replenishment in the SL. The vertical optical depth of the layer is simply $\kappa\Sigma$, where κ is opacity. Here, we set κ to Thomson electron scattering opacity for Solar metallicity, $\kappa_T \simeq 0.34 \text{ cm}^2 \text{ g}^{-1}$.

The problem has a complex hierarchy of timescales, starting with the dynamical scale (1), that is normally the smallest. Local thermal timescale depends on the effective and internal temperatures. For LMXBs, in Z and brighter atoll states, mass accretion rates span the range $10^{15} - 10^{18} \text{ g s}^{-1}$ ($10^{-11} - 10^{-8} M_\odot \text{ yr}^{-1}$) that implies effective temperatures of the order

$$\begin{aligned} T_{\text{eff}} &\simeq \left(\frac{GM\dot{M}}{8\pi\sigma_{\text{SB}}R_*^3} \right)^{1/4} \\ &\simeq 0.8 \left(\frac{M}{1.4 M_\odot} \right)^{1/4} \left(\frac{R_*}{12 \text{ km}} \right)^{-3/4} \left(\frac{\dot{M}}{10^{17} \text{ g s}^{-1}} \right)^{-1/4} \text{ keV}. \end{aligned} \quad (4)$$

Internal temperature, T_{in} , is about a factor $(\kappa\Sigma)^{1/4} \sim 100$ times larger, if $\Sigma \sim 10^8 \text{ g cm}^{-2}$ is taken as a representative value.

Thermal timescale is then easy to estimate in the gas-pressure-dominated case as

$$\begin{aligned} t_{\text{thermal}} &\sim \frac{E}{Q^-} \sim \frac{kT_{\text{in}}}{m_p \Sigma \sigma T_{\text{eff}}^4} \\ &\sim 10 \frac{\Sigma}{10^8 \text{ g cm}^{-2}} \left(\frac{T_{\text{in}}}{100 \text{ keV}} \right) \left(\frac{T_{\text{eff}}}{1 \text{ keV}} \right)^{-4} \text{ s}, \end{aligned} \quad (5)$$

where Q^- represents the energy lost via radiation (introduced more rigorously in Sect. 2.6). If energy release is close to balance with radiation losses, effective temperature does not change strongly, and most of the variations of the above quantity are related to the energy stored by gas and trapped radiation. Thermal and dynamical timescales become comparable if the surface density is small, $\Sigma \lesssim 100 \text{ g cm}^{-2}$.

The challenge of SL simulations for the case of LMXBs is in the relatively long accretion timescale. While the phenomena like kHz QPOs manifest themselves on dynamical timescales of milli- and microseconds, accretion rate is relatively stable at the scales of minutes to hours (viscous times of the inner disc), and the putative time of mass growth and depletion in a SL is apparently of the same order. These time scales are, however, much longer than both the thermal and dynamical time scales.

Hence, all the dynamical- and thermal-timescale phenomena we intend to consider appear in fact in a quasi-stationary SL where mass accreted during the considered timescales is negligibly small. However, to reach such an equilibrium state, one needs to simulate either an episode of much more rapid accretion or, alternatively, accretion atop of a much thinner atmosphere, where the surface densities of pre-existing and newly accreted material would be comparable on a reasonable time span of the simulation run. We try both approaches.

2.2. Geometry

We use a spherical system of coordinates consisting of radial coordinate r , colatitude θ , and longitude φ . Instead of θ , latitude $\lambda = \pi/2 - \theta$ will be used for visualization. The system is aligned with the rotation of the star, but is itself non-rotating (inertial). The SL is considered thin in radial direction, making r in a sense a vertical coordinate, along which hydrostatic equilibrium is assumed to hold. See Sect. 2.4 for more details.

2.3. Mass conservation

Continuity equation for density ρ and velocity \mathbf{v} , in the most general Newtonian form, is

$$\frac{\partial \rho}{\partial t} = -\nabla \cdot (\rho \mathbf{v}) + \text{source/sink terms}. \quad (6)$$

Integration over r yields

$$\frac{\partial \Sigma}{\partial t} = -\nabla \cdot (\Sigma \mathbf{v}) + S^+ - S^-, \quad (7)$$

where S^\pm are the source and sink terms for surface density. The source term is set explicitly as an inclined belt (to account for the case when the disc is inclined with respect to the NS)

$$S^+ = S_{\text{norm}}^+ e^{-(\cos \alpha / \cos \alpha_0)^2 / 2}, \quad (8)$$

where α is the angular distance from the direction of adopted disc rotation axis,

$$\cos \alpha = \cos \theta \cos i + \sin \theta \sin i \cos \Delta\varphi, \quad (9)$$

¹ <https://github.com/pabolmasov/SLayer>

where disc inclination i with respect to the spin axis of the star and $\Delta\varphi$ set the coordinates of the symmetry axis of the source.

Adding a sink allows to limit the growth of the mass of the SL and approach a quasi-stationary state. Matter existing long enough on the surface of the NS should adopt its velocity and physical properties. As our model adopts a simplified vertical structure, adding a sink allows to draw an effective boundary between the SL and the material of the NS. In this paper, we ignore the sink term, but include it into the equations for future use in the form

$$S^- = \frac{\Sigma}{t_{\text{depl}}}, \quad (10)$$

where t_{depl} is a depletion timescale set explicitly. This form is valuable for its simplicity and allows to study the role of the mass of the SL by considering gradual depletion regime (mass accretion is switched off but the sink is not) and the steady-state spreading regime by turning simultaneously on both the source and the sink. The processes responsible for depletion are probably non-linear and rather suggest an upper limit for Σ than a universal timescale, that may be included in further, more sophisticated versions of the model.

We also use a tracer quantity a to separate the contributions of the pre-existing and newly accreted material. It is assumed to be a passive scalar quantity transferred with the flow and initially equal to 0. The source of this quantity is designed in a way to reproduce the evolving fraction of newly accreted matter,

$$\frac{\partial a}{\partial t} + (\mathbf{v} \cdot \nabla) a = (1 - a) \frac{S^+}{\Sigma}. \quad (11)$$

2.4. Vertical structure

In the vertical (radial) direction, SL is supported by thermal (gas and radiation) pressure together with the relevant centrifugal force component. As we consider the vertical extent of the SL to be infinitely small, the timescale of vertical dynamical relaxation should also be small, hence we neglect the effect of radial velocity in momentum and energy equations. This allows to write down a hydrostatic balance equation

$$\frac{1}{\rho} \frac{\partial p}{\partial r} = -g_{\text{eff}} = -\frac{GM}{r^2} + \frac{v_\theta^2 + v_\varphi^2}{r}, \quad (12)$$

that needs to be supplemented by another equation to calculate simultaneously the vertical profiles of pressure and density. Let us assume, following Inogamov & Sunyaev (1999) and Suleimanov & Poutanen (2006), that the heat is released at the bottom of the SL, and the optical depth is high enough to use radiation diffusion approximation. Hence radiation flux F is constant with height

$$F = -\frac{c}{\kappa\rho} \frac{\partial p_{\text{rad}}}{\partial r}, \quad (13)$$

where p_{rad} is radiation pressure. Total pressure is assumed to be contributed by p_{rad} and gas pressure p_{gas} . Together, equations (12) and (13) imply constant pressure ratio $\beta = p_{\text{gas}}/p$ as long as opacity is constant with height. Hence, gas, radiation, and total pressure scale with each other, and the gas-to-total pressure ratio equals

$$\beta = 1 - \frac{\kappa F}{c g_{\text{eff}}}. \quad (14)$$

Proportionality of pressures also implies $p \propto \rho T \propto T^4$, that leads to $p \propto \rho^{4/3}$, an effectively polytropic law. This implies a relation between the pressure p_0 and density ρ_0 at the bottom of the SL and the corresponding vertically integrated quantities, pressure $\Pi = \int p dr$ and surface density $\Sigma = \int \rho dr$,

$$\Pi = \frac{4}{5} \frac{p_0}{\rho_0} \Sigma. \quad (15)$$

Constancy of β allows also to link surface energy density $E = \int \varepsilon dr$ (where ε is the volumetric energy density) and integrated pressure Π with each other. Energy density locally may be expressed as

$$\varepsilon = 3 \left(1 - \frac{\beta}{2}\right) p, \quad (16)$$

that implies an identical relation for the vertically integrated quantities

$$E = 3 \left(1 - \frac{\beta}{2}\right) \Pi. \quad (17)$$

The pressure ratio itself may be found as a function of E (or Π) and Σ . At the bottom of the layer,

$$\beta = \frac{\rho_0 k T_0}{m p_0} = \frac{k}{m} \frac{\rho_0}{p_0} \left(\frac{3}{4} \frac{c}{\sigma_{\text{SB}}} (1 - \beta) p_0 \right)^{1/4}, \quad (18)$$

where $m \simeq 0.6 m_p$ is the mean mass of a massive particle, that allows to solve implicitly for β , taking into account the expression for $p_0 = g_{\text{eff}} \Sigma$ arising as a solution to (12) and equation (17) and substituting them into (18):

$$\frac{\beta}{(1 - \beta)^{1/4} (1 - \beta/2)} = \frac{12}{5} \frac{k}{m} \left(\frac{3}{4} \frac{c}{\sigma_{\text{SB}}} g_{\text{eff}} \Sigma \right)^{1/4} \frac{\Sigma}{E}. \quad (19)$$

2.5. Momentum equations

We start with Euler equations with additional source and sink terms related to the momentum of the matter being accreted and to the friction between the SL and NS surface. Their general vector form is

$$\frac{\partial \mathbf{v}}{\partial t} + (\mathbf{v} \cdot \nabla) \mathbf{v} = -\frac{1}{\rho} \nabla p + \mathbf{g} + \text{source and sink terms}, \quad (20)$$

where \mathbf{g} is gravity without the contribution of centrifugal force, assumed directed along the radius vector. At the same time, the surface of the NS is close to being equipotential and thus is deformed due to rotation (we neglect all the other sources of deformation like magnetic fields and non-equilibrium stresses in the crust) that makes the polar-angle component $g_\theta = -\frac{1}{r} \frac{\partial \Phi}{\partial \theta}$, where Φ is gravitational potential, non-zero even after vertical integration. However, we will consider this component small $g_\theta \ll g_r$.

The radial component of the momentum equation reduces to the hydrostatic equation considered in Sect. 2.4. The two tangential components of the equation are convenient to re-write in terms of the two scalar quantities normally used in shallow-water approximation, vorticity

$$\omega = [\nabla \times \mathbf{v}]_r = \frac{1}{r \sin \theta} \left(\frac{\partial}{\partial \theta} (v_\varphi \sin \theta) - \frac{\partial v_\theta}{\partial \varphi} \right) \quad (21)$$

and divergence

$$\delta = (\nabla \cdot \mathbf{v}) = \frac{1}{r \sin \theta} \left(\frac{\partial}{\partial \theta} (v_\theta \sin \theta) + \frac{\partial v_\varphi}{\partial \varphi} \right). \quad (22)$$

Multiplying (20) by ρ and integrating over the total vertical extent of the SL yields

$$\frac{\partial \mathbf{v}}{\partial t} + (\mathbf{v} \cdot \nabla) \mathbf{v} = -\frac{1}{\Sigma} \nabla \Pi + \mathbf{g} + \text{source and sink terms.} \quad (23)$$

Detailed derivation of the equations for vorticity and divergence is given in Appendix A.

Taking the radial curl component of equation (23) results in an equation for vorticity

$$\begin{aligned} \frac{\partial \omega}{\partial t} + \nabla \cdot (\omega \mathbf{v}) &= -\nabla \times \frac{\nabla \Pi}{\Sigma} + (\omega_d - \omega) \frac{S^+}{\Sigma} \\ &+ \left[(\mathbf{v}_d - \mathbf{v}) \times \nabla \frac{S^+}{\Sigma} \right]_r + \frac{1}{t_{\text{fric}}} (2\Omega_{\text{NS}} \cos \alpha - \omega), \end{aligned} \quad (24)$$

where Ω_{NS} is the angular frequency of the star. Here, the last term describes viscous coupling between the SL and the surface of the NS. Our lack of knowledge about the nature and strength of this coupling is included in the unknown friction timescale t_{fric} . Preceding terms containing S^+ appear due to accretion of matter with given vorticity $\omega_d = 2\Omega_{\text{K}} \sin \alpha$ (where α is given by Eq. 9). In addition to this, the right-hand side of the equation includes a baroclinic term $\nabla \times \frac{\nabla \Pi}{\Sigma}$ equal to zero if a fixed equation of state is adopted, or if the distributions of pressure and density are exactly axisymmetric. This term can create vorticity through entropy variations.

Taking divergence of (23) provides an equation for δ

$$\begin{aligned} \frac{\partial \delta}{\partial t} &= [\nabla \times (\omega \mathbf{v})]_r - \nabla^2 \left(\frac{v^2}{2} + \Delta \Phi \right) - \nabla \cdot \left(\frac{1}{\Sigma} \nabla \Pi \right) \\ &- \delta \frac{S^+}{\Sigma} + (\mathbf{v}_d - \mathbf{v}) \cdot \nabla \frac{S^+}{\Sigma} - \frac{\delta}{t_{\text{fric}}}. \end{aligned} \quad (25)$$

The term $\Delta \Phi = \frac{1}{2} \Omega_{\text{NS}}^2 R_*^2$ originates from the rotational deformation of the neutron star.

2.6. Energy conservation

In general form, energy conservation implies (Suleimanov & Poutanen 2006):

$$\frac{\partial}{\partial t} \left(\frac{1}{2} \rho v^2 + \varepsilon \right) + \nabla \cdot \left(\left[\frac{1}{2} \rho v^2 + \varepsilon + p \right] \mathbf{v} \right) = q_{\text{NS}} + q^+ - q^-, \quad (26)$$

where the right-hand side accounts for heat exchange with the neutron star (q_{NS}), heat released within the layer (q^+), and radiation losses q^- . After integration, all the q quantities will result in corresponding capital Q quantities: fluxes through the surface and energy release per unit area.

We treat the hydrodynamics of the SL as ideal, though the numerical solution techniques used (described later in Sect. B) provide dissipation at small scales close to the spatial resolution used. If momentum transfer is dominated by turbulent motions forming a direct cascade similar to Kolmogorov cascade (Monin et al. 2007) where energy is transferred from larger to smaller scales, the exact nature and properties of the viscous dissipation at the small scales are irrelevant. However, conservation of energy implies that viscous dissipation should act as an additional source of internal energy. All the kinetic energy lost by the flow should reappear as heat. We will assume this heat to appear at the bottom of the flow and to diffuse upwards leaving the SL from its upper surface.

Taking into account momentum conservation, friction, and viscous dissipation, and integrating the energy equation vertically, we end up with the equation

$$\frac{\partial E}{\partial t} + \nabla \cdot (E \mathbf{v}) = -\delta \Pi + Q^+ - Q^- + Q_{\text{NS}} + Q_{\text{acc}}, \quad (27)$$

where Q^+ is the heat released in the spreading layer, Q_{NS} is the heat received from the neutron star, Q^- is the radiation flux lost from the surface, and the additional term Q_{acc} corresponds to the thermal energy introduced with the accreting matter and released during its mixing with the pre-existing material. Vertically integrated pressure and energy are related by (17). Dissipation is calculated as kinetic energy lost by the flow

$$Q^+ = -\Sigma \mathbf{v} \cdot \frac{d\mathbf{v}}{dt} \Big|_{\text{dissipation}}, \quad (28)$$

while the energy radiated away from the surface is set by radiation energy diffusion (see Sect. 2.4)

$$Q^- = \frac{c g_{\text{eff}}}{\kappa} (1 - \beta), \quad (29)$$

where κ is the Rosseland average opacity we consider equal to Thomson scattering opacity, $\kappa = \kappa_{\text{T}} \approx 0.34 \text{ cm}^2 \text{ g}^{-1}$. If β approaches zero, the SL becomes a ‘‘levitating layer’’ supported mainly by radiation pressure (Inogamov & Sunyaev 1999). For $\beta \ll 1$, the energy loss term is essentially independent of the physical conditions inside the layer.

Additional terms related to the accreting matter are more difficult to constrain from the physical point of view. It is natural to assume that the initial temperature of the newly introduced material is non-zero, and hence the increase in surface density is accompanied with an increase in surface energy density as well. Besides, as the velocities of the accreting and the pre-existing matter are in general different, some of the kinetic energy is dissipated during the process of mixing (the exact physical mechanism could be kinetic, hydrodynamic, or MHD). Energy and momentum conservation laws predict that the amount of dissipated energy per unit accreted mass is $(\mathbf{v}_d - \mathbf{v})^2/2$, hence

$$Q_{\text{acc}} = \left(\left(\frac{E}{\Sigma} \right)_d + \frac{1}{2} (\mathbf{v}_d - \mathbf{v})^2 \right) S^+, \quad (30)$$

where index ‘‘d’’ refers to the quantities in the disc (and thus, in the matter entering the SL).

2.7. Initial conditions

Simplest possible initial conditions are constant surface density and pressure in combination with rigid-body rotation. This may be achieved if the rotation rate is exactly equal to the rotation frequency of the NS, Ω_{NS} , and the deformation of the NS exactly compensates the centrifugal forces. Configuration is stable and may survive for simulation times vastly exceeding the durations of the runs used in this work. In Sect. B.2.1, we use this initial condition configuration to check the numerical stability and dissipation of our numerical scheme.

Vorticity of a rigid-body rotation is

$$\omega_{\text{init}} = 2\Omega_{\text{NS}} \cos \theta. \quad (31)$$

As the motions are limited to pure rotation, initial divergence is strictly zero. To the basic initial condition set, a small (five per cent) perturbation was added in a form of an over- or under-density. The perturbation is designed as an entropy variation not affecting the background pressure distribution.

Table 1. Spreading layer simulations.

Model ID	dimensions	t_{\max} s	Σ_{init} g cm^{-2}	\dot{M} $M_{\odot} \text{ yr}^{-1}$	PDS ^a s	comments
3LR	128×256	0.5	10^8	10^{-3}	0.35–0.5	
3HR	256×512	0.08	10^8	10^{-3}		
3LRinc	128×256	0.6	10^8	10^{-3}	0.4–0.6	$i = \pi/4$
8LR	128×256	0.32	10^4	10^{-8}	0.27–0.32	
8HR	256×512	0.07	10^4	10^{-8}		
3LRoff	128×256	1.0	10^8	0	0.5–0.68	starts with the end of 3LR

Notes. ^(a) Integration limits for calculations of the PDS.

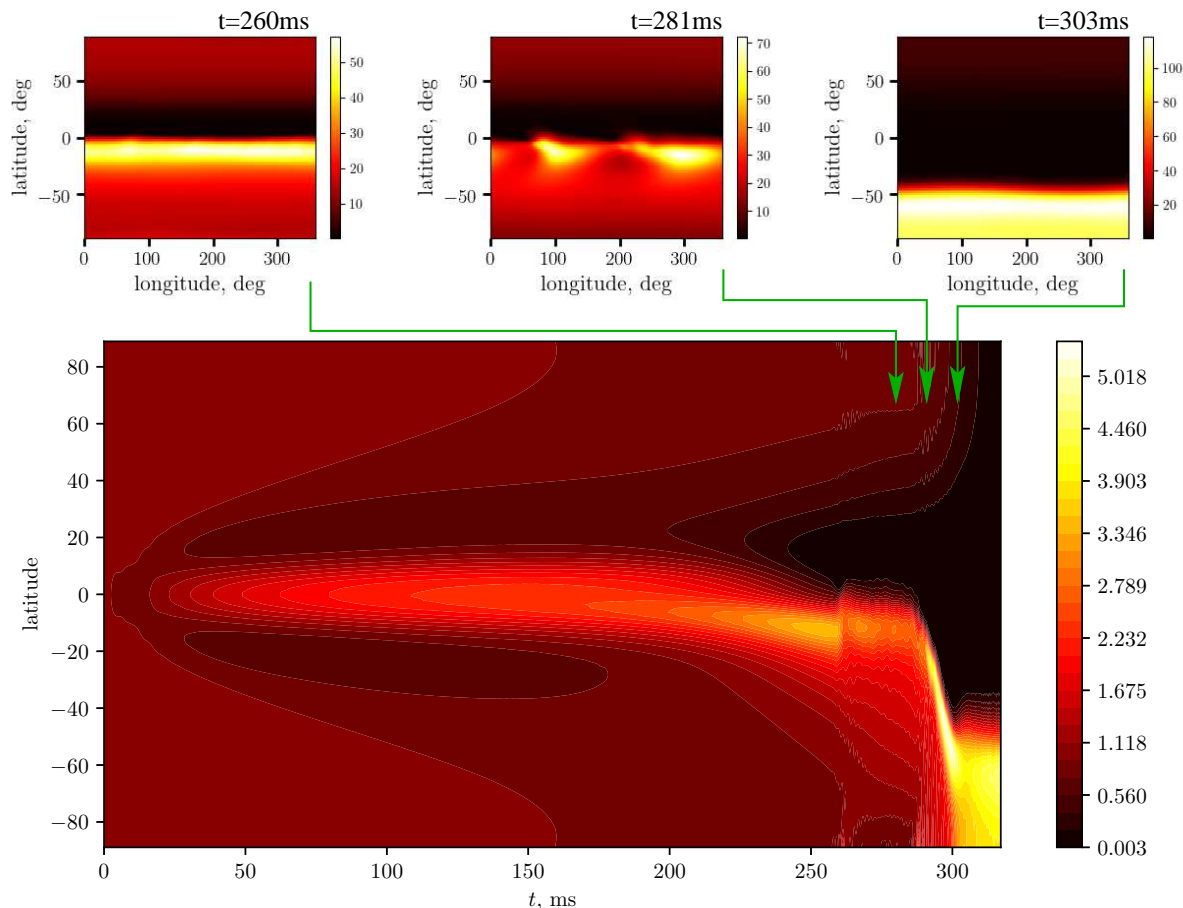


Fig. 1. Time-latitude diagram for longitudinally-averaged surface density logarithm in the realistic-accretion-rate 8LR simulation. Note the decrease in surface density at latitudes about $\pm 20^\circ$ ($t \approx 50\text{--}100\text{ms}$) due to heating, the gradual north-south symmetry breaking between $t \approx 200$ and 250 ms and later dynamical-timescale evolution. Upper panels show three snapshots of surface density during the later stages of the heating instability development. Surface density is in 10^4 g cm^{-2} in all the panels, the scale is linear for the snapshots and logarithmic for the time-latitude diagram.

3. Results

3.1. Model setup

For the detailed description of the numerical techniques used to perform the simulations in this work, see Appendix B. There, we also describe the tests for numeric performance, stability, and accuracy. We list all the SL models calculated for this paper in Table 1. Letters “LR” and “HR” in a simulation ID always refer to “low” (128×256) or “high” (256×512) resolution. Consistency between the corresponding low- and high-resolution runs is an important test for numerical effects (noise and diffusion). Below,

we describe the setups of all these models, while the description of the results is given in the following subsections.

All the models include a NS rotating with a spin period $P_{\text{spin}} = 3 \text{ ms}$. Initially, all the matter on the surface rotates together with the star as a rigid body. As we so far do not include any friction with the NS surface, rotation of the star affects the results only through the initial conditions and the deformation of the stellar surface (potential term in Eq. 25).

Most models include a mass source corresponding to a steady-state accretion from a thin disc. To avoid strong velocity gradients causing high-frequency noise, the mass accretion

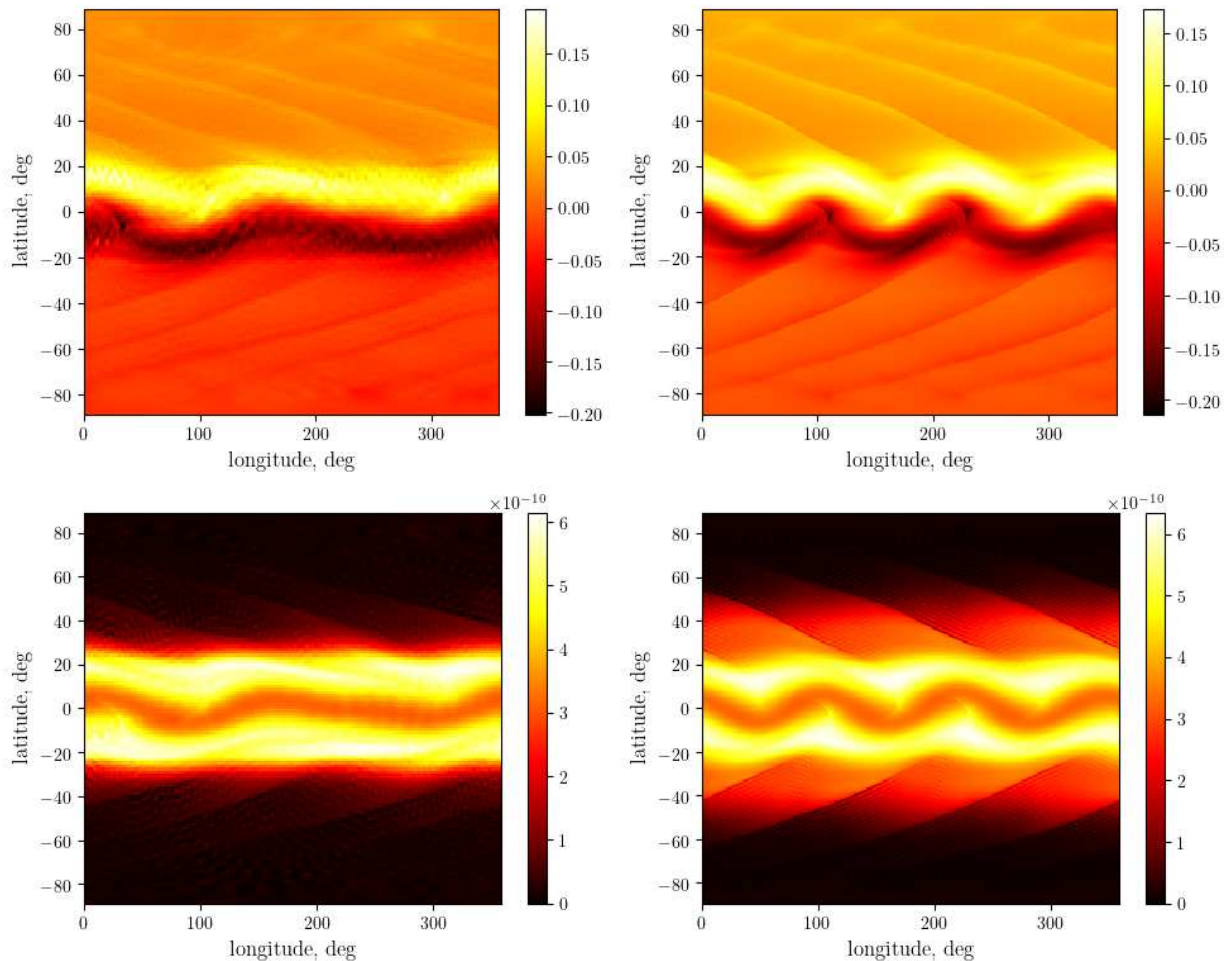


Fig. 2. Resolution effects after $t = 0.03$ s (ten spin periods) of evolution for the high-accretion-rate models 3LR (low numerical resolution; left panels) and 3HR (high numerical resolution; right panels). Vorticity maps on the top, emitted radiation flux (Q^-) map on the bottom panels. Spectral simulations are able to capture the oblique wave patterns and “curling” of the equatorial spreading layer belt even with the low numerical resolution runs. For the high-resolution runs, more fine-scale substructure starts to appear.

rate approaches the steady-state value smoothly, following the exponential law

$$\dot{M}(t) = \dot{M}_0 \left(1 - e^{-t/t_{\text{turn-on}}}\right), \quad (32)$$

where the turn-on timescale was set to $10P_{\text{spin}}$ for all the simulations.

As the timescales observed in real LMXBs differ by six orders of magnitude, it is difficult to perform a single realistic simulation resolving the dynamic-time-scale variability for a time span sufficient to see the changes in the SL structure. We use two approaches to avoid this difficulty: first, we consider “enhanced accretion” with $\dot{M} = 10^{-3} M_{\odot} \text{ yr}^{-1} \simeq 6 \times 10^{20} \text{ g s}^{-1}$ (models 3LR and 3HR); secondly, we consider accretion on top of a thin layer with $\Sigma_0 = 10^4 \text{ g cm}^{-2}$. Both tricks shorten the effective evolution timescales by several orders of magnitude. We expect the hydrodynamics to work about the same in both configurations though the radiation timescales are vastly different.

As an alternative to both these approaches, we calculate a model reproducing the evolution of a spreading layer after switching off the mass source (model 3LRoff). It starts with the final snapshot of 3LR and then gradually cools down for another 0.5 s. Finally, in the model 3LRinc, we consider the case when the source is inclined with respect to the initial rotation plane.

3.2. General properties

For the simulations with accretion, no quasi-stationary picture is expected to be achieved, as we do not consider any sinks in our simulations. However, heating and velocity gradients created by accretion lead to at least two important dynamical effects relevant for the dynamics of SLs. In the two groups of simulations, with “enhanced” and “normal” mass accretion rate, two different instabilities emerge. For the realistically low mass accretion rate ($\dot{M} = 10^{-8} M_{\odot} \text{ yr}^{-1}$) and low initial surface density ($\Sigma_0 = 10^4 \text{ g cm}^{-2}$), the equatorial belt forming out of the accreting matter during the first milliseconds of accretion is cooled efficiently, and most of the subsequent dissipation takes place at higher latitudes, where the newly added material mixes with the old, slowly rotating NS atmosphere. This results in a *heating instability*: local displacement of the cool equatorial belt material leads to increased dissipation on the opposite side of the equator, that results in a pressure gradient increasing the initial displacement. This is easily seen in Fig. 1, where the later-time evolution (starting at approximately $t \sim 0.2$ s) is marked by a gradual, and then dynamical-timescale development of a strong mass asymmetry between the southern and the northern hemispheres. Development of the instability also breaks the axial symmetry, especially during the period of rapid evolution.

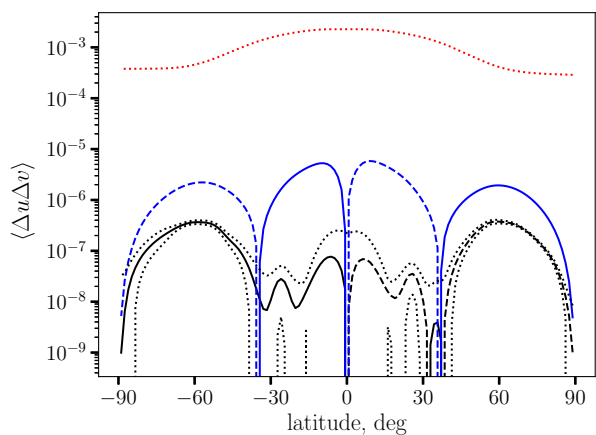


Fig. 3. Azimuthally- and temporally-averaged dynamical quantities for the high-accretion-rate model 3LR. Visualized quantities are Reynolds stress (black), mean velocity product $v_\theta v_\varphi$ (blue), and sound velocity (red dotted) as functions of co-latitude θ . All the quantities were averaged over the period of time between 0.1 and 0.3 s, and over the azimuthal angle. Solid lines correspond to positive quantities (northward motion or momentum transfer), dashed to negative (southward). Dotted black curves show the 1-sigma standard deviation interval for the Reynolds stress. Reynolds stress is small in comparison to pressure but surprisingly stable in its sign, showing a clear poleward angular momentum transfer.

At the same time, for the case of enhanced accretion, cooling and heating timescales are much longer, and all the observed dynamical effects are purely hydrodynamical. They are reasonably reproduced by the low-resolution simulations, though increasing resolution reveals more details and adds regularity to the observed turbulent patterns (see Fig. 2).

3.3. Angular momentum transport within the layer

Large-accretion-rate models 3LR and 3HR demonstrate a system of oblique waves generated by the velocity discontinuity. In the new, rapidly rotating, part of the flow, a system of standing waves rapidly evolves into a non-linear regime, forms a non-axisymmetric wobble structure seen in Fig. 2, that is subsequently smeared off. At large latitudes, where the old, slowly rotating matter dominates, the waves create a correlation between orthogonal velocity components. Velocity correlation provides a Reynolds stress component

$$T_{\theta\varphi} = \langle \Sigma(v_\theta - \langle v_\theta \rangle)(v_\varphi - \langle v_\varphi \rangle) \rangle, \quad (33)$$

where angular brackets $\langle \dots \rangle$ denote averaging in time and longitude. In Fig. 3, we show the value of $T_{\theta\varphi}$, calculated for the model 3LR for the period of time 0.1–0.3 s after the start. While the SL itself apparently approach a quasi-stationary axisymmetric state at the timescale of about 1s, higher latitudes still show variability and non-axisymmetry up to the end of the simulation. In real astrophysical sources, the mass accretion rate is variable on sub-second timescales, meaning that, even if the Reynolds stress is a reaction on the variations in mass accretion rate, it should always be present.

Existence of a hydrodynamical stress, small but significant, suggests a long local viscous timescale corresponding to oblique-wave-mediated angular momentum transfer. Near the poles, Reynolds' stress partially compensates the advective angular momentum flow caused by compression of the pre-existing

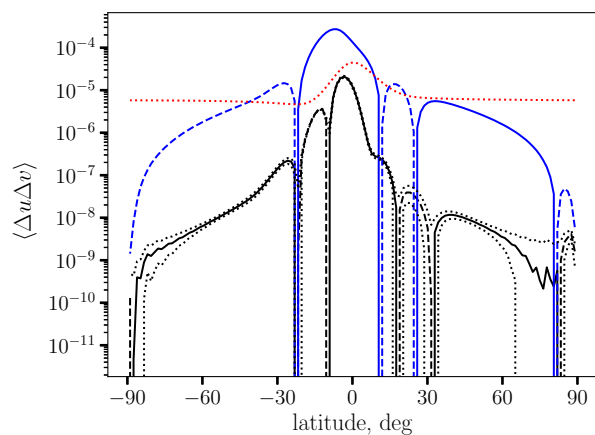


Fig. 4. Azimuthally- and temporally-averaged dynamical quantities for the realistic-accretion-rate model 8LR. Symbols and quantities are the same as in Fig. 3. Averaging was performed from $t = 0.2$ to 0.28 s, when the initial hemisphere asymmetry is developed due to heating instability.

polar cap material. Near the equator, at the same time, both advection and viscous transport of angular momentum are directed polewards.

For the realistic-accretion-rate models 8LR and 8HR, heating instability creates a strong flow of mass toward one of the poles. At the profound stage of this process, when most of the accumulated mass flips to one side, axial symmetry is broken, that effectively creates a very large Reynolds stress spreading the angular momentum of the rapidly rotating matter over latitudes (see Fig. 4). Reynolds stress rapidly removes the angular momentum from the equatorial stream in both directions (note the sign change near -10° latitude).

3.4. Artificial light curves

To produce artificial light curves, we use a simplified approach ignoring all the relativistic effects. We choose an inclination of the observer i_{obs} and integrate the bolometric flux Q^- emitted from the surface

$$L_{\text{obs}} = 4 \int_{\alpha_{\text{obs}} < \pi/2} Q^- \cos \alpha_{\text{obs}} R^2 \sin \theta d\theta d\varphi, \quad (34)$$

where

$$\cos \alpha_{\text{obs}} = \cos \theta \cos i_{\text{obs}} + \sin \theta \sin i_{\text{obs}} \cos \varphi \quad (35)$$

and α_{obs} is the angle at which the surface element is seen by an observer located in the colatitude i_{obs} and azimuthal angle $\varphi = 0$ in the spherical coordinate system. Such an approach allows to reproduce the effects of visibility of any moving features on the surface of the star. The factor 4 in Eq. (34) allows to interpret L_{obs} as isotropic luminosity, equal to the actual luminosity for an isotropic source.

Power density spectra (PDS) were calculated using the standard FFT algorithm (Cooley & Tukey 1965) with fractional normalization. If the light curve is set as a series of observed luminosities L_k at the equidistant instances of time t_k , the Fourier amplitude is found as a function of frequency f as

$$PDS(f) = \left| \frac{\sum_k L_k e^{-2\pi i f t_k}}{\sum_k L_k} \right|^2 \simeq \left| \frac{\int L e^{2\pi i f t} dt}{\int L dt} \right|^2. \quad (36)$$

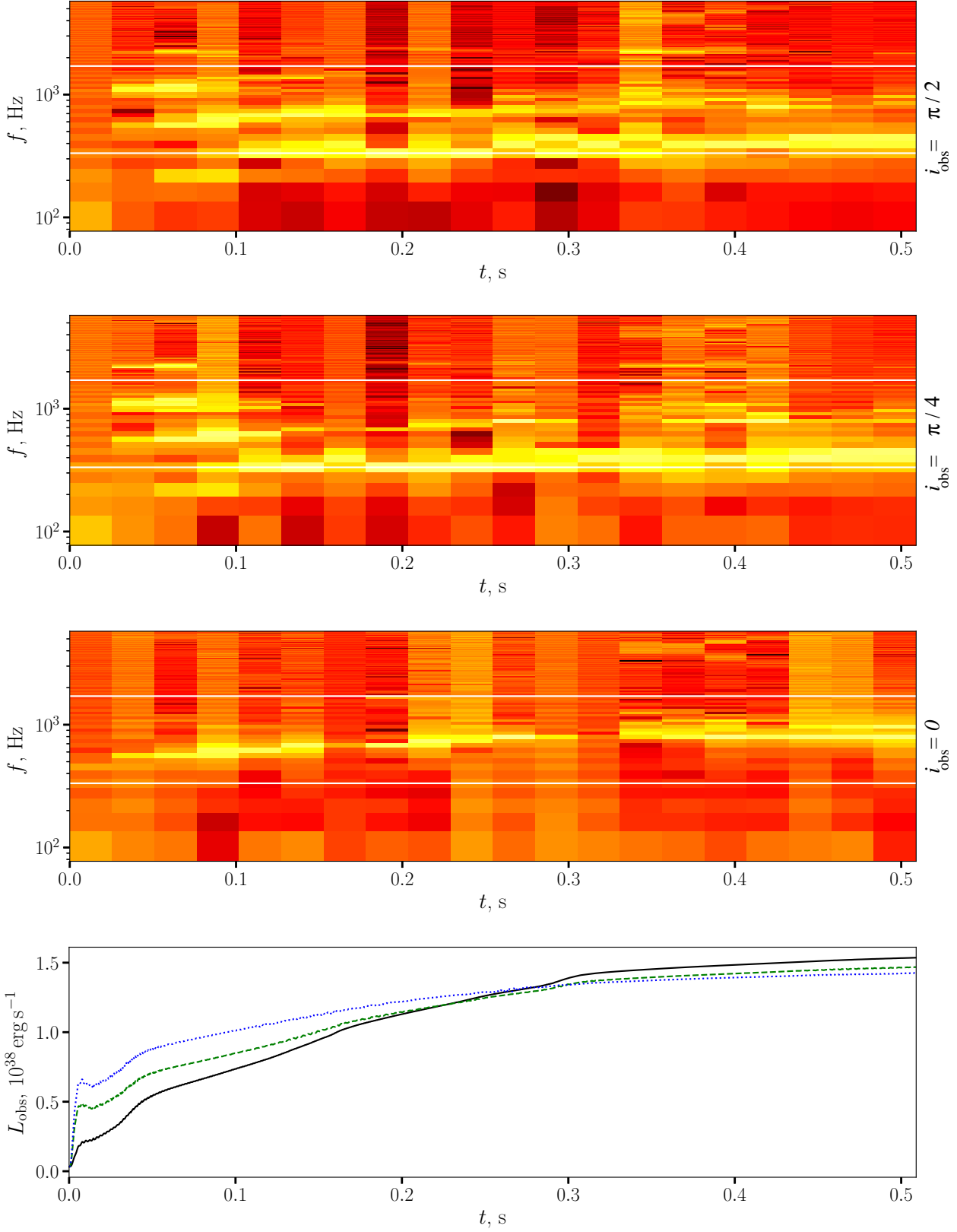


Fig. 5. Dynamical PDSs for the “observed flux” quantity calculated as described in Sect. 3.4 for the high-accretion-rate model 3LR. The three upper panels show dynamical spectra for the observer’s inclinations of $\pi/2$, $\pi/4$, and 0, respectively. White horizontal lines show the spin (lower) and Keplerian frequencies. Lowermost panel shows the corresponding light curves: $i_{\text{obs}} = \pi/2$, $\pi/4$, and 0 cases are shown with blue dotted, green dashed, and black solid lines. Several oscillation modes are visible, one of them for a pole-on observer. Their frequencies evidently correlate with the flux. See text for more discussion.

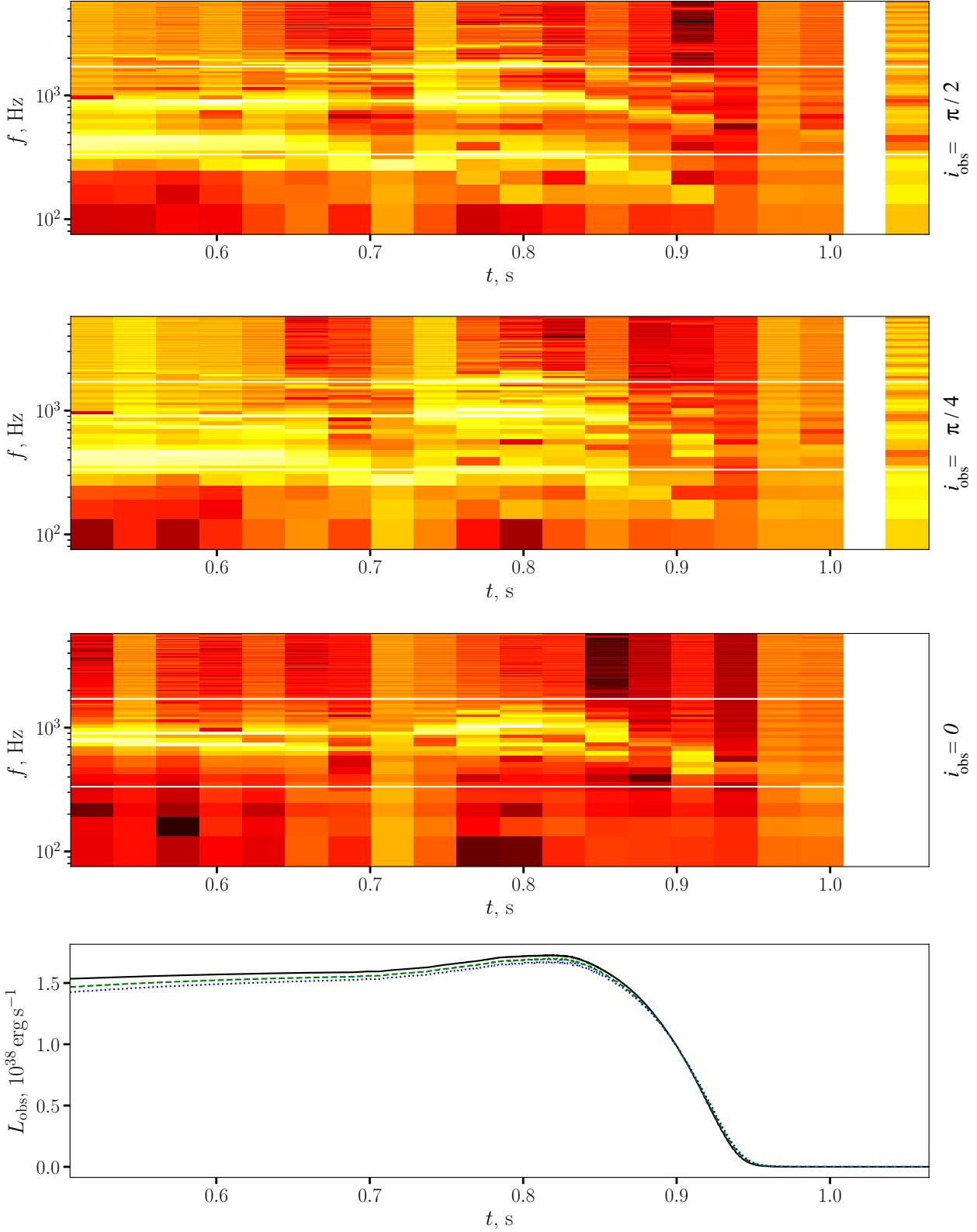


Fig. 6. The same as Fig. 5, for the model with a turned-off mass source, 3LRoff.

The frequency grid on which the PDS is calculated is equally spaced with $\Delta f = 1/T$, where T is the time span. Spectral power defined this way is a measure of the relative amplitude of a variability mode. For a broad spectral peak, variability amplitude may be estimated as $\sim \sqrt{\sum \Delta PDS}$, where ΔPDS stands for the

excess spectral power associated with the particular spectral detail, and summation is done over the relevant spectral interval.

In Fig. 5 we show the dynamic (calculated inside 20 separate time bins) power-density spectra calculated for different i_{obs} . Most of the non-axisymmetric structures in this simulation

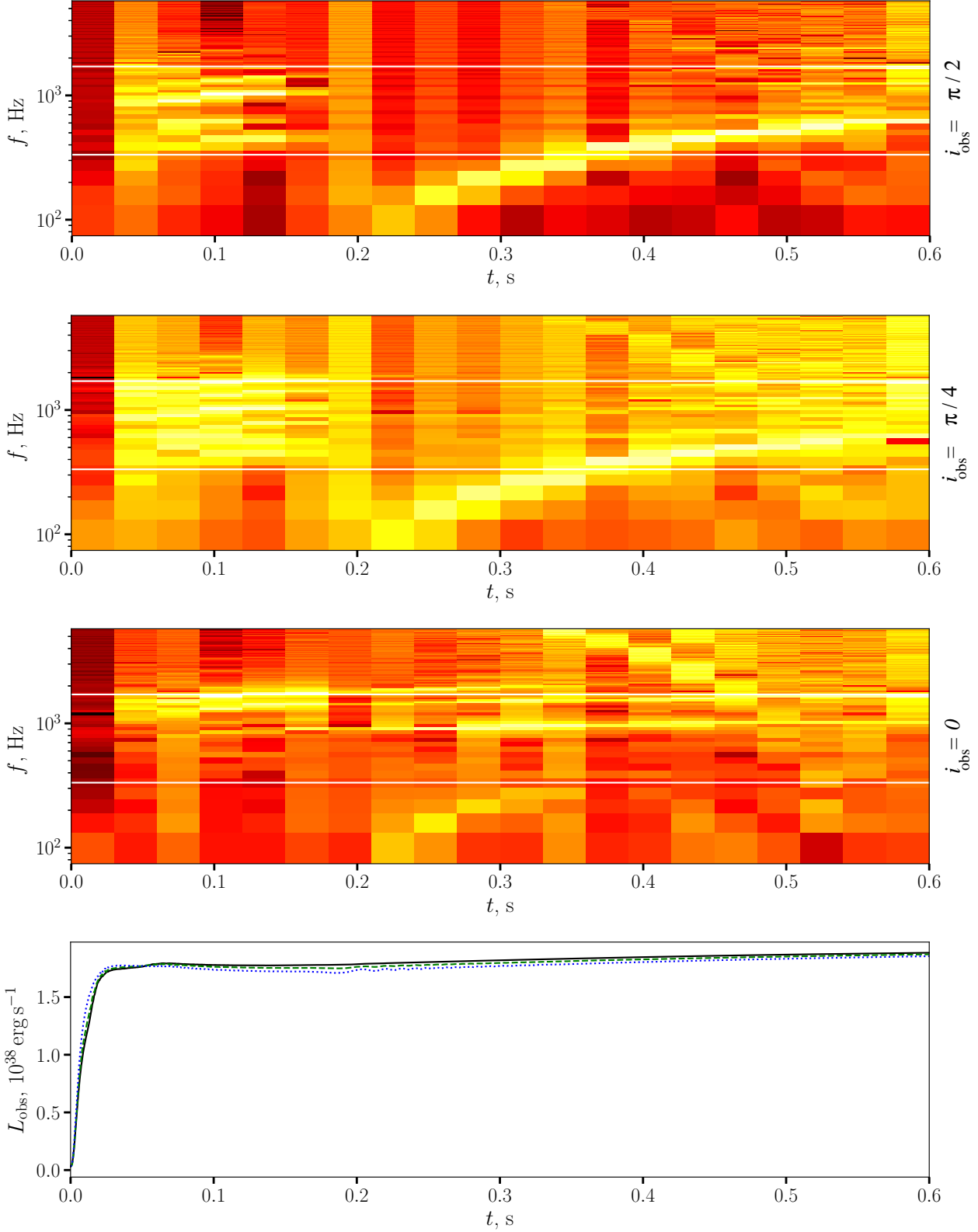


Fig. 7. The same as Fig. 5 but for the model with an inclined source, 3LRinc.

are moving slightly faster than the star itself: their contribution is visible just above Ω_{NS} . There is also power at about double spin frequency and, in the very beginning, near the third harmonic. The contribution seen during the first ~ 0.1 s of the simulation may be attributed to the initial perturbation rotating at the

spin frequency. For a polar observer, however, very little variability is seen save for a single peak initially close to $1.5\Omega_{\text{NS}}$ and then gradually increasing its frequency towards 700–800 Hz. This signal is visible for all the inclinations but in general is weaker than the rotating modes. The properties of this mode fit

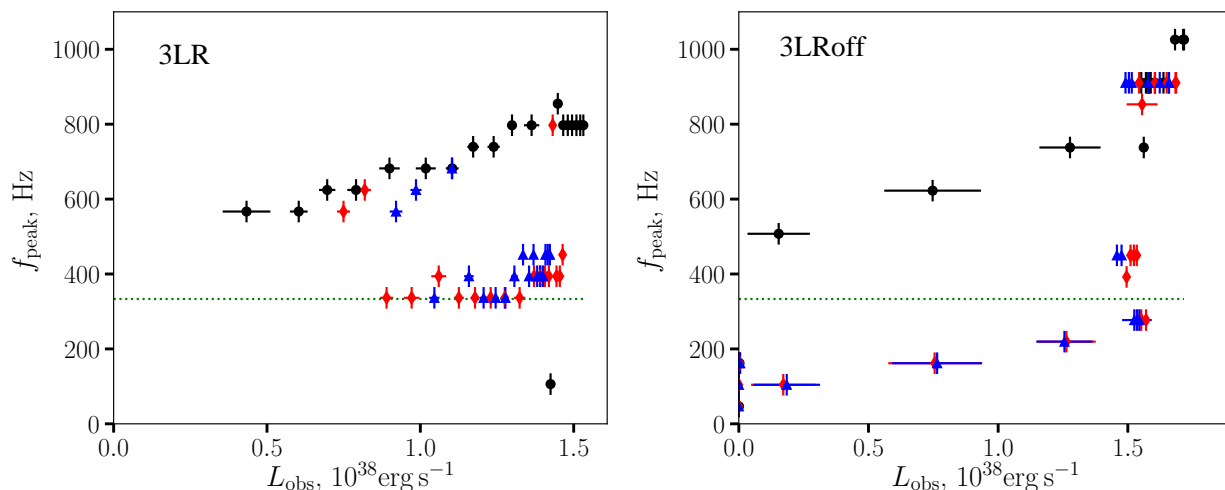


Fig. 8. Peak frequency (calculated as the position of the maximum of $f \times PDS$) as a function of observed luminosity (calculated using expression 34) for $i_{\text{obs}} = 0$ (black circles), $\pi/4$ (red diamonds), and $\pi/2$ (blue triangles). Simulation runs 3LR (left) and 3LRoff (right). Error bars show flux dispersion within the time bin and the size of the frequency bin where the maximum was detected. Horizontal dotted green lines show spin frequency. Evolution of the peak frequency in the simulations is seen to reproduce the observed positive correlation with the flux.

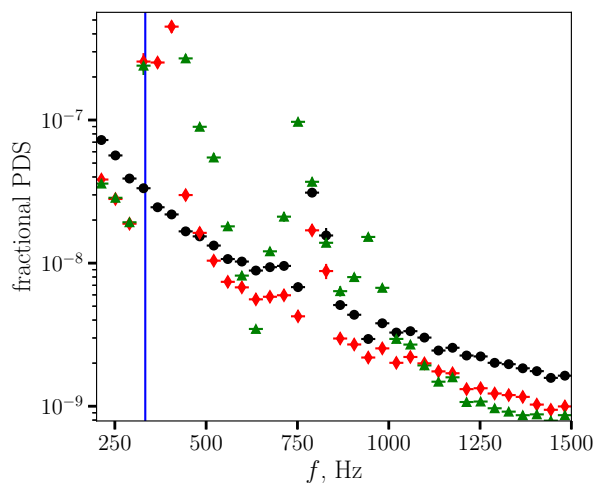


Fig. 9. Integral PDS (time span 0.2 to 0.5 s) of the simulation 3LR for different inclinations. Black dots correspond to a pole-on observer $i_{\text{obs}} = 0$, red diamonds to the intermediate inclination of $i_{\text{obs}} = \pi/4$, and green triangles to $i_{\text{obs}} = \pi/2$.

well to the concept of a latitudinally propagating surface wave moving in a waveguide, similar to the modes considered by Piro & Bildsten (2004a). We discuss the implications of such an interpretation later in Sect. 4.

In Fig. 6 we show how the dynamic PDS changes when rapid accretion stops (model 3LRoff, that starts with the end of simulation 3LR). The quasi-periodic features around two-three spin frequencies retain at least for the period when the layer remains hot (before $t \simeq 0.95$ s). The non-rotating mode is evidently split into two QPO features. A hint of such a split is visible also at $t \sim 0.3\text{--}0.4$ s in Fig. 5. All the characteristic features, as in the original simulation with accretion, correlate with flux.

Peak frequencies in the dynamical PDSs are shown in Fig. 8 as functions of flux. There is an evident signal for the pole-on simulated light curve both in the original model with enhanced accretion, and in the switch-off simulation. The non-rotating mode discussed above dominates for the pole-on case, for which

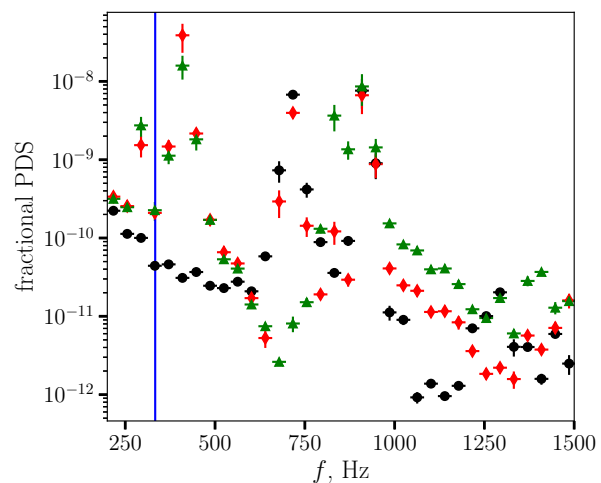


Fig. 10. Same as Fig. 9, but for the simulation 3LRoff and between $t = 0.58$ and 0.67 s.

a clear correlation between flux and frequency is observed. For an inclined observer, rotating modes are stronger. Interestingly enough, inclined source is capable of exciting variability modes with frequencies lower than the spin frequency.

We also consider PDSs integrated over time intervals where the shapes of dynamic PDSs remain relatively stable and/or show hints of additional spectral features. In Fig. 9, we show such a spectrum for the 3LR simulation, computed for $t = 0.2\text{--}0.5$ s. Pole-on PDS is dominated by a single narrow peak at about 800 Hz. At large inclinations, this single QPO transforms into two, and an additional peak emerges at about one spin frequency. For 3LRoff, splitting of the main mean peak for $i_{\text{obs}} = 0$ is visible at $t \sim 0.5\text{--}0.7$ s (shown in Fig. 10) and later at $t \sim 0.8$ s. Later, the structure of the layer starts rapidly changing due to rapid cooling and switching to the gas-pressure-dominated regime.

For the inclined simulation 3LRinc (Fig. 7), there is an early stage ($0\text{--}0.2$ s) of the collision of the two flows inclined to each other. Then, a quasi-axisymmetric configuration forms, and the variability pattern becomes similar to those of the aligned mod-

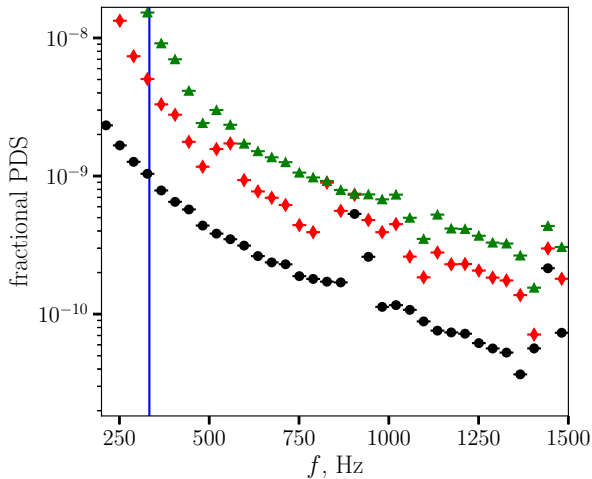


Fig. 11. Same as Fig. 9, but for the simulation 3LRinc and for the time span $t = 0.35 - 0.5$ s.

els discussed above. Unlike the aligned case, the observed luminosity changes in very narrow limits, probably because the size of the SL is now determined by the geometry of the inflow rather than by angular momentum transfer. Dissipation is smoothly distributed over the whole latitude range between $-i$ and i , and saturates at a level $Q^- \simeq cg_{\text{eff}}/\kappa_{\text{T}}$. The apparent luminosity seen by a pole-on observer is

$$\begin{aligned} L_{\text{obs, inc}} &\simeq \frac{4cg_{\text{eff}}R_*^2}{\kappa} \int_{\pi/2 < \theta < i} \cos \theta \sin \theta d\theta \int_0^{2\pi} d\varphi \\ &\simeq \frac{4\pi cg_{\text{eff}}R_*^2}{\kappa} \cos^2 i \simeq 10^{38} \text{ erg s}^{-1}. \end{aligned} \quad (37)$$

Starting from $t \simeq 0.15$ s, the pole-on PDS shows one stable peak at about 1 kHz and a hint of another peak at about 1.5 kHz, sometimes split in two (see Fig. 11 showing the PDS integrated over the integral 0.4–0.65 s; similar picture is seen for $t \sim 0.2 - 0.3$ s). Unlike the aligned case, rotating modes at later stages appear slower than non-rotating. Probably, this is related to the overall change in angular momentum of the layer that is affected by the pre-existing matter rotating in different direction.

For the realistic mass-accretion-rate configuration, oscillations appear simultaneously with the development of the heating instability, and their contribution is clearly visible only at particular inclinations (see Fig. 12). The two poles behave in a profoundly different way because of the asymmetry formed by heating instability. Further simulations of the 8LR case are difficult because of the very strong density contrasts formed during the instability.

4. Discussion

In the dynamical spectra presented in Sect. 3.4, there are clearly at least two types of quasi-periodic variability signals: one disappears for a pole-on observer and is thus related to non-axisymmetric structures (waves and vortices produced by shear instabilities). The other is present at all inclinations. The frequency of this mode clearly increases with the flux, approximately as $f_{\text{QPO}} \propto L_{\text{obs}}^{1/3}$ (see Fig. 8). We leave a detailed study of the properties of the predicted QPOs to a separate paper.

It is natural to interpret this oscillation mode as a surface mode existing within the SL, as it was done by Piro & Bildsten

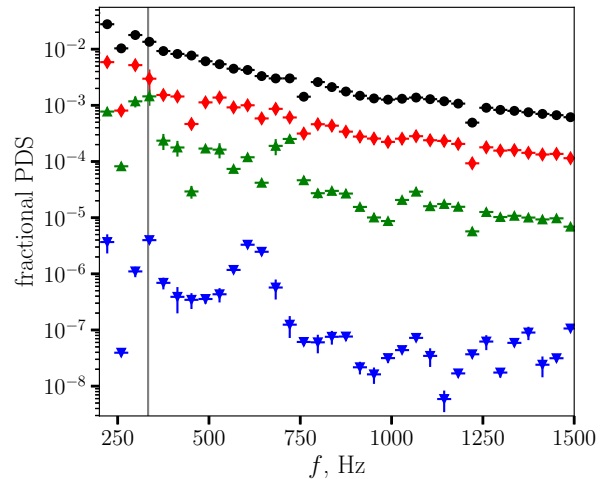


Fig. 12. Integral PDS (time span from 0.27 to 0.32 s) for the simulation 8LR for different inclinations (black circles $i_{\text{obs}} = 0$, red diamonds $i_{\text{obs}} = 45^\circ$, green upward triangles $i_{\text{obs}} = 90^\circ$, and blue downward triangles $i_{\text{obs}} = 180^\circ$).

(2004a) for dwarf-nova oscillations (DNO). However, the width of the SL practically independently of the assumptions should increase with mass accretion rate. This is especially true for the radiation-pressure-supported case when the radiative flux is fixed by balance with effective gravity $F = cg_{\text{eff}}/\kappa$, and the growth of the area over which the dissipation is spread should reflect the growth of the mass accretion rate. Approximately, the width of the SL grows linearly with the mass accretion rate, $H \propto \dot{M}$. As the speed of sound depends weakly on the mass accretion rate, the frequency of a DNO-like sonic mode for a thin radiation-pressure-supported SL

$$f_s \sim \frac{1}{2\pi} \frac{c_s}{H} \propto \dot{M}^{-1}. \quad (38)$$

This approach, however, assumes that the observed oscillations are produced near the equator. Equatorial belt is indeed responsible for most of the energy dissipation, but the radiation flux is, due to the importance of radiation pressure, broadly distributed over the surface, and most of the variability comes from high latitudes (see Fig. 13). Besides, the SL itself can not work as a proper waveguide: velocity shears are very strong, larger than the Keplerian frequency itself.

We can only conclude that the oscillations present in the observational data and in simulations are not the resonance frequencies for sonic waves but rather correspond to a different type of oscillations. The best candidate for these oscillation modes are r-modes, or Rossby waves. As we show in Appendix C, their frequencies at a given co-latitude θ form an equidistant spectrum with

$$f_{r,m} = \frac{1}{2\pi} (\Omega_e + m\Omega), \quad (39)$$

where

$$\Omega_e = \sqrt{2\Omega \frac{\partial}{\partial \theta} (\Omega \sin^2 \theta)} \quad (40)$$

is the epicyclic frequency (the frequency in latitudinal direction of a portion of matter conserving its angular momentum and affected by gravity and inertial forces only), $\Omega = \Omega(\theta)$ is the rotation frequency, and m is a whole number. For rigid-body rotation, $\Omega_e \simeq 2\Omega \cos \theta$. If the variability is excited in a slowly

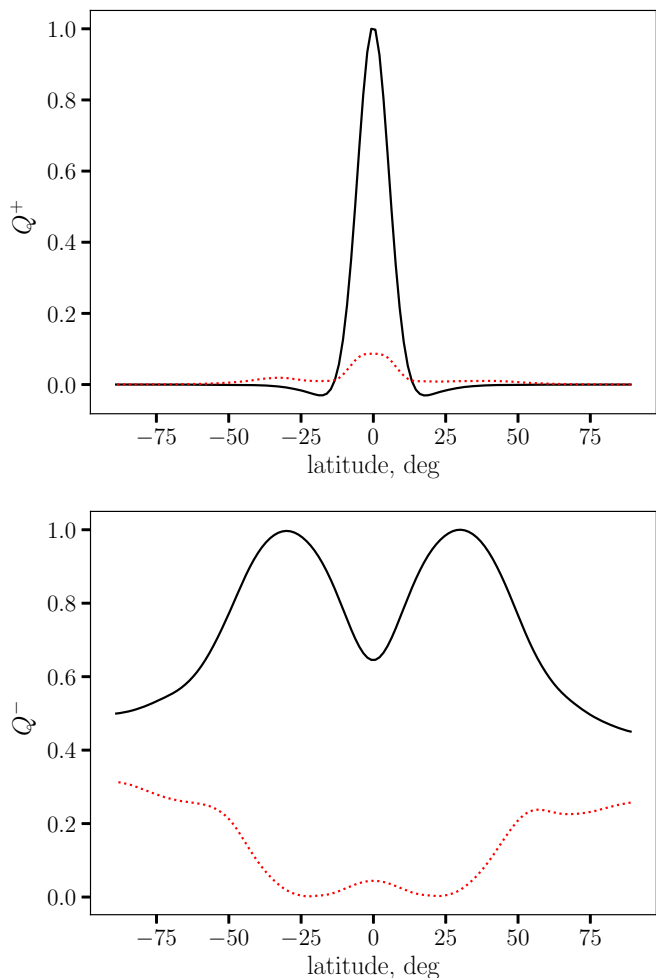


Fig. 13. Time- and longitude-averaged energy dissipation (upper panel) and radiation flux (lower panel) for the high-accretion-rate 3LR simulation run. Mean values and root-mean-square deviations are shown, respectively, with black solid and red dotted curves. In each panel, the relevant quantity is normalized by the maximal averaged value. Most of the dissipation in the system takes place directly at the equator whereas the escaping radiation flux peaks at higher latitudes near the upper and lower rims of the SL.

rotating region outside the SL itself, and the epicyclic frequency changes slowly throughout this region, we get one peak corresponding to the non-rotating mode at $f \lesssim 2f_{\text{spin}}$ and aliases at frequencies differing by $\Delta f \approx f_{\text{spin}}$. This is similar to the spectra obtained in our simulations (see Sect. 3.4), and at the same time similar to the pair QPOs in LMXBs. As seen in Fig. 14, there is a maximum of epicyclic frequency roughly in the interaction region between the SL and the slowly rotating matter. Besides, the epicyclic frequency in this region is very close to the local rotation frequency, meaning that the perturbations are in resonance with rotation. As most variability comes from higher latitudes, we propose that the oscillations are excited at intermediate latitudes (30 – 50° for 3LR), probably by shear instabilities in the interaction region, and then propagate towards the poles.

Let us assume that the oscillations are always generated at the latitude of the rim of the SL, all the energy is dissipated within the layer, and the flux locally equals the Eddington flux $c g_{\text{eff}}/\kappa$. Flux scaling with the Eddington limit means that the luminosity should grow approximately linearly with the surface area of the layer, $L \approx L_{\text{Edd}} \cos \theta_{\text{SL}}$. Then the epicyclic frequency

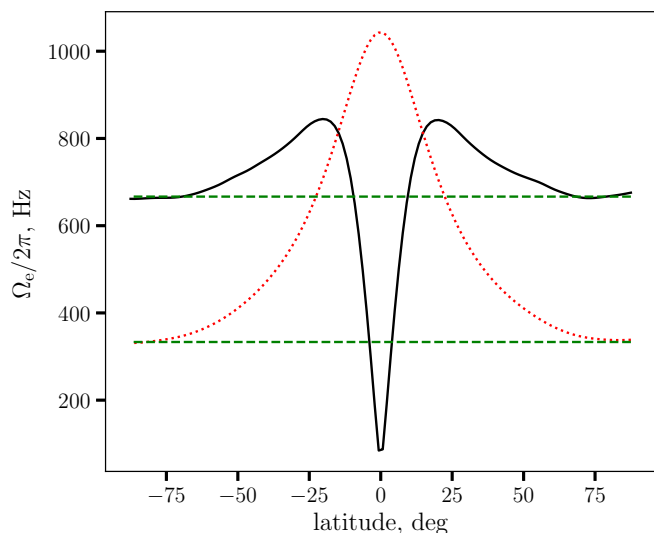


Fig. 14. Epicyclic (black solid) and local rotation (red dotted) frequencies for the model 3LR, averaged in time between 0.3 and 0.5 s and over the azimuthal angle. Green dashed horizontal lines correspond to the rotation rate of the NS and its second harmonic. Maximum of the epicyclic frequency is located near the upper and lower rims of the SL where the equatorial layer interacts with the slowly rotating matter the most strongly. Local rotation frequency is also of the same order in these locations making it easy for all kinds of perturbations to resonate with the rotating background fluid.

should scale as

$$f_{\text{r0}} \approx 2f_{\text{spin}}\theta_{\text{SL}} \approx 2f_{\text{spin}}\frac{L}{L_{\text{Edd}}}, \quad (41)$$

that reproduces the characteristic values of the frequency in our simulations but somewhat over-estimates the dependence on flux. As the radiating region does not exactly coincide with the SL, and the width of the SL also depends on the parameters of the inflow (the extreme case being the case of a strongly inclined source, see above Eq. 37), and g_{eff} is generally smaller than gravity, we expect the linear scaling to be a very crude approximation, over-predicting the slope of the actual (seen in simulations) frequency dependence on flux.

Similar type of a QPO spectrum consisting of the local epicyclic frequency and its aliases with the rotation frequency was obtained by Erkut et al. (2008) who considered a BL as a part of the accretion disc. However, neither this model nor our simulations are so far capable of explaining clearly why only two peaks are observed in the PDSs of real LMXBs, and one in a large number of LMXBs, the distance between the peaks is actually half of the spin frequency. Explaining and predicting the details of QPO features in the PDS requires more profound studies, both analytical and numerical. Both classical and spreading layer approaches have their limitations, as the real motions are likely to be three-dimensional (Babkovskaia et al. 2008).

5. Conclusions

In this paper, we considered a time-dependent hydrodynamic SL on the surface of a NS. We used two-dimensional spectral modelling to resolve the evolution of the differentially rotating flow. We find that, though challenging due to the super-sonic compressible nature of the flow, spectral simulations of a SL on the surface of a NS may be quite productive. We mainly consider

the interaction of a new material rotating close to Keplerian velocity with the old, spun-down atmosphere of the NS, and this interaction produces a set of hydrodynamical phenomena having a huge impact on the dynamics of the system. In particular, the velocity shear is susceptible to shear instability modes that provide angular momentum transfer within the layer and excite inertial oscillation modes closer to the poles, where they produce variability patterns closely resembling kHz QPOs in real LMXB systems.

Acknowledgements. We would like to thank Alexander Philippov for his help with the spectral filtering, and Roman Rafikov for discussions about the different oscillation modes. We also thank Yuri Levin, Andrei Beloborodov, Andrei Gruzinov, Lorenzo Sironi, Joe Patterson, and Anatoly Spitkovsky for discussions on the different aspects of boundary layer physics. PA acknowledges the support from the Program of development of M.V. Lomonosov Moscow State University (Leading Scientific School ‘Physics of stars, relativistic objects and galaxies’). JP was supported by the grant 14.W03.31.0021 of the Ministry of Science and Higher Education of the Russian Federation. We acknowledge the use of the Finnish Grid and Cloud Infrastructure and the Finnish IT Center for Science (CSC).

References

- Babkovskaia, N., Brandenburg, A., & Poutanen, J. 2008, *MNRAS*, 386, 1038
- Balbus, S. A. & Hawley, J. F. 1991, *ApJ*, 376, 214
- Belyaev, M. A. & Quataert, E. 2018, *MNRAS*, 479, 1528
- Belyaev, M. A. & Rafikov, R. R. 2012, *ApJ*, 752, 115
- Belyaev, M. A., Rafikov, R. R., & Stone, J. M. 2013, *ApJ*, 770, 67
- Cooley, J. W. & Tukey, J. W. 1965, *Math. Comput.*, 19, 297
- Courant, R., Friedrichs, K., & Lewy, H. 1928, *Mathematische Annalen*, 100, 32
- Erkut, M. H., Psaltis, D., & Alpar, M. A. 2008, *ApJ*, 687, 1220
- Gilfanov, M., Revnivtsev, M., & Molkov, S. 2003, *A&A*, 410, 217
- Gottlieb, D. & Shu, C.-W. 1997, *SIAM Rev.*, 39, 644
- Hasinger, G. & van der Klis, M. 1989, *A&A*, 225, 79
- Inogamov, N. A. & Sunyaev, R. A. 1999, *Astronomy Letters*, 25, 269
- Inogamov, N. A. & Sunyaev, R. A. 2010, *Astronomy Letters*, 36, 848
- Jakob-Chien, R., Hack, J., & Williamson, D. 1995, *J. Comput. Phys.*, 119, 164
- Kluźniak, W. & Abramowicz, M. A. 2001, *Acta Physica Polonica B*, 32, 3605
- Kluźniak, W., Abramowicz, M. A., Kato, S., Lee, W. H., & Stergioulas, N. 2004, *ApJ*, 603, L89
- Lamb, F. K., Shibazaki, N., Alpar, M. A., & Shaham, J. 1985, *Nature*, 317, 681
- Méndez, M. & Belloni, T. 2007, *MNRAS*, 381, 790
- Méndez, M., van der Klis, M., Ford, E. C., Wijnands, R., & van Paradijs, J. 1999, *ApJ*, 511, L49
- Méndez, M., van der Klis, M., & van Paradijs, J. 1998, *ApJ*, 506, L117
- Miller, M. C. & Lamb, F. K. 2016, *European Physical Journal A*, 52, 63
- Miller, M. C., Lamb, F. K., & Psaltis, D. 1998, *ApJ*, 508, 791
- Monin, A., Yaglom, A., & Lumley, J. 2007, *Statistical Fluid Mechanics: Mechanics of Turbulence*, Dover books on physics No. v. 1 (Dover Publications)
- Motta, S. E., Rouco Escorial, A., Kuulkers, E., Muñoz-Darias, T., & Sanna, A. 2017, *MNRAS*, 468, 2311
- Nättilä, J., Miller, M. C., Steiner, A. W., et al. 2017, *A&A*, 608, A31
- Papaloizou, J. C. B. & Stanley, G. Q. G. 1986, *MNRAS*, 220, 593
- Parfrey, K., Beloborodov, A. M., & Hui, L. 2012, *MNRAS*, 423, 1416
- Philippov, A. A., Rafikov, R. R., & Stone, J. M. 2016, *ApJ*, 817, 62
- Piro, A. L. & Bildsten, L. 2004a, *ApJ*, 616, L155
- Piro, A. L. & Bildsten, L. 2004b, *ApJ*, 610, 977
- Popham, R. & Narayan, R. 1995, *ApJ*, 442, 337
- Pringle, J. E. 1977, *MNRAS*, 178, 195
- Psaltis, D., Méndez, M., Wijnands, R., et al. 1998, *ApJ*, 501, L95
- Ray, T. P. 1982, *MNRAS*, 198, 617
- Rebusco, P. 2008, *New A Rev.*, 51, 855
- Revnivtsev, M. G. & Gilfanov, M. R. 2006, *A&A*, 453, 253
- Rincon, F., Ogilvie, G. I., & Cossu, C. 2007, *A&A*, 463, 817
- Schaeffer, N. 2013, *Geochemistry, Geophysics, Geosystems*, 14, 751
- Sibgatullin, N. R. & Sunyaev, R. A. 2000, *Astronomy Letters*, 26, 699
- Suleimanov, V. & Poutanen, J. 2006, *MNRAS*, 369, 2036
- Tikhonov, A. & Samarskii, A. 2013, *Equations of Mathematical Physics*, Dover Books on Physics (Dover Publications)
- van der Klis, M. 2000, *ARA&A*, 38, 717
- van der Klis, M. 2001, *ApJ*, 561, 943
- Vreugdenhil, C. B. 1990, *VKI, Computational Fluid Dynamics, Volume 1* 48 p (SEE N90-27989 22-34), 1
- Wijnands, R., van der Klis, M., Homan, J., et al. 2003, *Nature*, 424, 44
- Zhuravlev, V. V. & Razdoburdin, D. N. 2018, *A&A*, 619, A44

Appendix A: Derivation of the equations for divergence and vorticity

To get the equations for $\delta = \nabla \cdot \mathbf{v}$ and $\omega = [\nabla \times \mathbf{v}]_r$, we need to take divergence and curl of the system of dynamical equations containing sources and sinks

$$\frac{\partial \mathbf{v}}{\partial t} + (\mathbf{v} \cdot \nabla) \mathbf{v} = -\frac{1}{\rho} \nabla p + \mathbf{g} + \frac{\rho^+}{\rho} \mathbf{v}_{\text{source}} - \frac{\mathbf{f}_{\text{fric}}}{\rho}, \quad (\text{A.1})$$

where $\mathbf{g} = -\nabla\Phi$ is gravity without centrifugal terms, and then integrate them in radial direction. Gravitational potential has the form $\Phi = -\frac{GM}{R} + \Delta\Phi$, where $\Delta\Phi$ accounts for a non-spherical shape of the star and depends on the latitude and longitude. For the friction force \mathbf{f}_{fric} , we use the form $\mathbf{f}_{\text{fric}} = -\frac{1}{t_{\text{fric}}} (\mathbf{v} - \mathbf{v}_{\text{NS}})$.

Before deriving the actual equations for vorticity and divergence, note that

$$\mathbf{v} \times \boldsymbol{\omega} = \frac{1}{2} \nabla^2 \mathbf{v} - (\mathbf{v} \nabla) \mathbf{v}. \quad (\text{A.2})$$

Hence,

$$\nabla \times [\mathbf{v} \times \boldsymbol{\omega}] = -\nabla \times (\mathbf{v} \nabla) \mathbf{v}. \quad (\text{A.3})$$

Taking curl of (A.1) yields

$$\frac{\partial [\nabla \times \mathbf{v}]}{\partial t} + (\mathbf{v} \cdot \nabla) [\nabla \times \mathbf{v}] = (\boldsymbol{\omega} \cdot \nabla) \mathbf{v} - (\nabla \cdot \mathbf{v}) \boldsymbol{\omega} + \frac{1}{\rho^2} [\nabla p \times \nabla \rho] - \nabla \times \left(\frac{\rho^+}{\rho} \mathbf{v}_{\text{source}} \right) - \nabla \times \frac{\mathbf{f}_{\text{fric}}}{\rho}, \quad (\text{A.4})$$

where the curl of the inertial term is best expanded using Eqs. (A.2) and (A.3). Taking radial integral of the radial component of (A.4) is straightforward, as the equation does not contain radial derivatives. Finally, we get equation (24)

$$\frac{\partial \omega}{\partial t} + \nabla \cdot (\boldsymbol{\omega} \mathbf{v}) = -\nabla \times \frac{\nabla \Pi}{\Sigma} + (\omega_{\text{source}} - \omega) \frac{S^+}{\Sigma} + \left[(\mathbf{v}_d - \mathbf{v}) \times \nabla \frac{S^+}{\Sigma} \right]_r + \frac{1}{t_{\text{fric}}} (\omega_{\text{NS}} - \omega). \quad (\text{A.5})$$

The right-hand side of this equation contains a baroclinic term capable of creating vorticity out of density and pressure variations, and three terms related to the vorticity of the accreted matter ω_{source} and friction with the surface.

Another equation describing the time evolution of δ comes from taking divergence of dynamical equation. It is rather non-trivial to expand the advection term, $(\nabla \cdot ((\mathbf{v} \cdot \nabla) \mathbf{v}))$, therefore let us first note that, according to (A.3),

$$(\nabla \cdot [\mathbf{v} \times \boldsymbol{\omega}]) = \nabla^2 \frac{v^2}{2} - \nabla \cdot ((\mathbf{v} \cdot \nabla) \mathbf{v}). \quad (\text{A.6})$$

Here, the last term on the right-hand side is identical to the advective left-hand-side term in the derivative of equation (A.1), hence

$$\frac{\partial \delta}{\partial t} = (\nabla \cdot [\mathbf{v} \times \boldsymbol{\omega}]) - \nabla \cdot \left(\frac{\nabla \Pi}{\Sigma} \right) - \nabla^2 \left(\frac{v^2}{2} + \Delta\Phi \right) - \delta \frac{S^+}{\Sigma} + (\mathbf{v}_{\text{source}} - \mathbf{v}) \nabla \frac{S^+}{\Sigma} - \frac{\delta}{t_{\text{fric}}}. \quad (\text{A.7})$$

Potential term $\Delta\Phi$ appears because of rotational deformation of the star. As the surface of the star should be an equipotential surface, total gravitational and centrifugal potential

$$\Phi - \frac{1}{2} R^2 \Omega_{\text{NS}}^2 = -\frac{GM}{R} + \Delta\Phi - \frac{1}{2} R^2 \Omega_{\text{NS}}^2 = \text{const}, \quad (\text{A.8})$$

implying $\Delta\Phi = \frac{1}{2} R^2 \Omega_{\text{NS}}^2$.

Appendix B: Numerical implementation and tests

Appendix B.1: Code description

The problem we consider is essentially a more physically elaborate version of shallow-water hydrodynamics, supplemented with energy transfer and source and sink terms. As the problem is formulated for the surface of a sphere, it is natural to use a spectral code operating spherical harmonics. We used the `shtns` library (Schaeffer 2013) designed for hydrodynamical and geophysical applications². The challenge of our problem is that, unlike the classical shallow-water physics, it is far from the sub-sonic, Rossby-approximation motions, and thus the time step is limited by several processes. One of the requirements for the time step is the Courant-Friedrichs-Lewy condition (Courant et al. 1928) of the form

$$\Delta t \leq \Delta t_{\text{CFL}} = \frac{C}{u} \Delta x_{\text{min}}, \quad (\text{B.1})$$

² We also used a wrapper class `spharmt` (<https://gist.github.com/jswhit/3845307>) for `shtns` quantities and operators written by Jeffrey Whitaker.

where Δx_{\min} is the minimal physical size of a cell in the simulation domain, u is the fastest relevant signal propagation velocity, and $C \lesssim 1$ is a constant related to the particular solver used in simulations. Existence of sources and sinks for several physical quantities sets additional upper limits for the time step and requires adjusting the time step with the physical conditions. We compute the actual time step as a harmonic sum of several time steps

$$\Delta t = \left(\sqrt{C_{\text{sound}} c_{s, \max}^2 + C_{\text{adv}} v_{\max}^2} \Delta x_{\min}^{-1} + C_{\text{thermal}} \Delta t_{\text{thermal}}^{-1} + C_{\text{accr}} \Delta t_{\text{accr}}^{-1} \right)^{-1}, \quad (\text{B.2})$$

where $C_{\text{sound}, \text{adv}, \text{thermal}, \text{accr}} \lesssim 1$ are dimensionless adjusted parameters regulating the role of each timestep, and $\Delta t_{\text{thermal}} = \min \frac{E}{Q^+ + Q^-}$ and $\Delta t_{\text{accr}} = \min \frac{\Sigma}{\dot{S}^+ + \dot{S}^-}$ are the time steps required to resolve temporally thermal and accretion processes. Such a choice for a variable timestep ensures resolving all the relevant physical processes: sonic wave propagation, dissipation, radiation losses, and accretion.

As spectral methods tend to produce high-frequency noise, diffusion-like dissipation terms were introduced for all the five principal quantities ω , δ , Σ , E , and a . In the equation for some quantity x , a term $\left((\nabla^2)^{N_{\text{diss}}/2} x \right) / t_{\text{D}}$ was added to the right-hand side of the corresponding equation. In wavenumber space, this corresponds to cutting off higher frequencies by multiplying the spectrum by some degree N_{diss} of the factor corresponding to Laplacian. In the numerical implementation of equations (7), (24), (25), and (27), dissipation terms were added. The timescale t_{D} is assumed to scale with the time step Δt that allows to fix the form of the dissipation multiplier in spectral space. In spectral space, dissipation term we use may be viewed as a multiplier

$$D = e^{-L N_{\text{diss}}/2 \frac{\Delta t}{t_{\text{D}}}}, \quad (\text{B.3})$$

where $L = -l(l+1)/R_*^2$ is the Laplacian acting on the spherical harmonic of degree l (see Tikhonov & Samarskii 2013), and $N_{\text{diss}} \geq 2$ is a free parameter describing the shape of the low-pass filter. If $N_{\text{diss}} = 2$, the filtering procedure is equivalent to a regular diffusion term added to the right-hand sides of all the main differential equations. The flow as a whole is negligibly affected if the dissipation factor for the lowest-order harmonic is indistinguishable from zero $t_{\text{D}} \gtrsim |\ln e_{\text{M}}| \Delta t$ (Parfrey et al. 2012), where e_{M} is machine precision.

Effectively, filtering with $N_{\text{diss}} > 2$, while more efficient than normal diffusion, cuts very sharply all the high frequencies. Such spectral truncation leads to its own noise, especially close to discontinuities. This is known as Gibbs phenomenon (Gottlieb & Shu 1997) and leads to oscillations that may be amplified by the non-linear nature of our system of equations. For Σ and E that can vary sharply and span several orders of magnitude, but become unphysical if negative, Gibbs phenomenon may become disastrous. A reasonable solution introducing little Gibbs effect and providing an extremely accurate treatment to the large-scale flow is

$$D = e^{-L \left(L + \frac{1}{R_*^2} \right) \frac{\Delta t}{t_{\text{D}}}}, \quad (\text{B.4})$$

that we use for most of the simulations in this paper.

The energy lost by the flow is added as a source of internal energy, as described in Sect. 2.6. By adding dissipation as a source of energy, we are likely to introduce high-frequency noise to the energy field, hence the dissipation field was smoothed in the same way as the basic quantities (see Eq. B.3), but with a shorter diffusion time scale. The exact value of the dissipation smoothing parameter affects the thermal stability of the simulation but does not change the overall dynamics. From the physical point of view, it only ensures that the dissipation does not significantly vary within a single resolution element.

The code itself is written as a hybrid PYTHON3/C++ program. All the numerically heavy (spectral) calculations are solved with the C++ SHTNS library, whereas the main loop and the related high-level functionalities are operated from the more user-friendly PYTHON3 driver. In our experience, this provides a good balance between numerical efficiency and easiness of use. The spherical harmonic calculations are parallelized using the shared memory paradigm with OPENMP pragmas. This enables us to take advantage of multi-core platforms ranging from powerful desktop computers to occupying one complete node in computing clusters. The Hierarchical Data Format (HDF5) is used to save and store the simulation results.

Appendix B.2: Tests

In Table B.1, we list the test models we calculated with their basic parameters.

Appendix B.2.1: Zero-accretion-rate, rigid-body rotation case

As one of the tests, we try evolution of a layer with initial surface density $\Sigma_0 = 10^8 \text{ g cm}^{-2}$ and sound velocity $c_s \simeq 1.7 \times 10^{-3} c$ without accretion or depletion. As in all the other models, an initial perturbation of 5% was introduced. Spin period was set to 3 ms. Mach number of this flow is about 50. For this test, we also turn off dissipation heating and radiation losses. Without thermal effects, rotation profile in such a model should not change with time, and the perturbation proceeds rotating with the surface of the star. To check the accuracy of this solution, it is sufficient to correct for the rotation angle, interpolate from one grid to another, and estimate the standard deviation or the maximal deviation between the map calculated by the code and the interpolated initial map.

Fig. B.1 shows how the maximal relative difference in surface density evolves with time. The errors around 10^{-3} are interpolation errors. As we can see, supersonic rotation is reasonably well tracked for multiple rotation periods, and the accuracy is better for a finer grid.

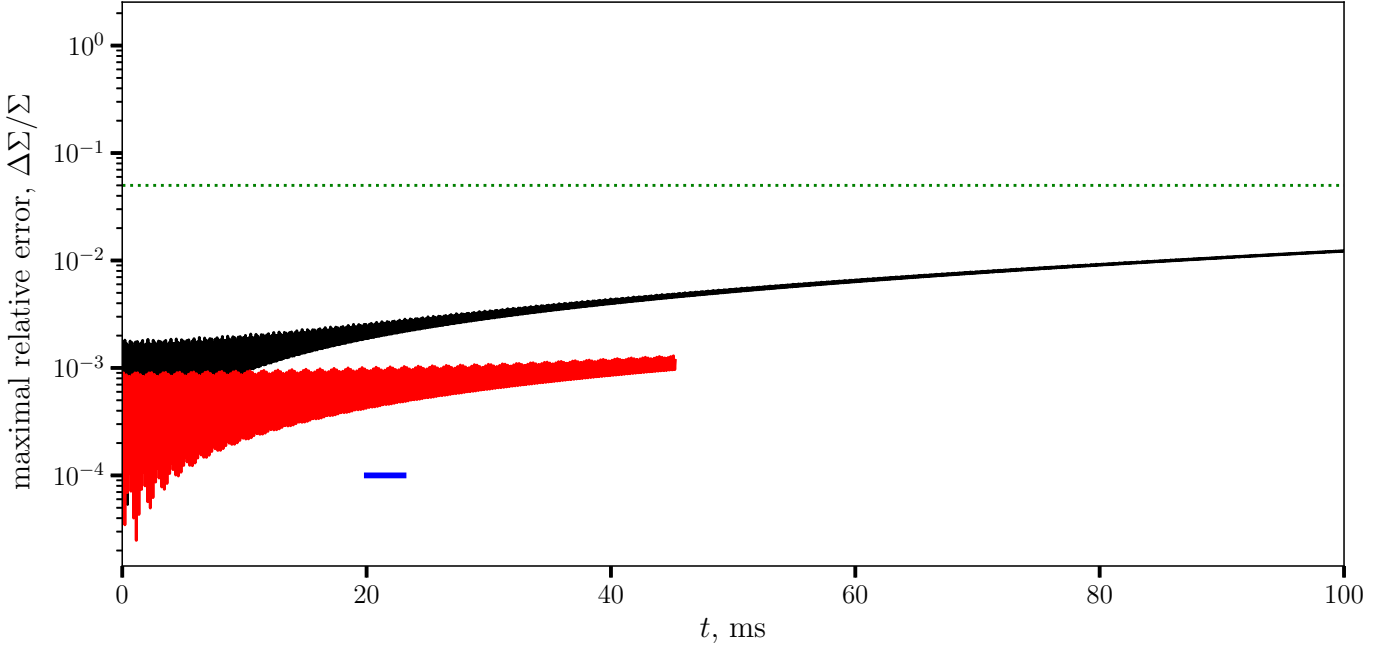


Fig. B.1. Maximal relative error in surface density $\max \frac{\Delta \Sigma}{\Sigma}$ for the test models NDLR (black) and NDHR (red). The blue horizontal segment in the lower panel has the length of one spin period. The dotted green horizontal line corresponds to the amplitude of the initial perturbation, 0.05.

Table B.1. Test simulations.

Model ID	dimensions	t_{\max} s	Σ_{init} g cm^{-2}	P_{spin} ms	comments
NDLR	128×256	0.1	10^8	3	
NDHR	256×516	0.04	10^8	3	
twistLR	128×256	0.15	10^8	30	sub-sonic twist test
twistHR	256×512	0.15	10^8	30	sub-sonic twist test
stwistLR	128×256	0.04	10^8	10	super-sonic twist test
stwistHR	256×512	0.03	10^8	10	super-sonic twist test

Appendix B.2.2: Split-sphere tests

The purpose of this test set (twistLR, twistHR, stwistLR, and stwistHR) was to trace the development of sub- and super-sonic shear instabilities on a sphere. Rigid-body rotation ($P_{\text{spin}} = 10$ and 30 ms) was modified by a factor rapidly changing from -1 to 1 near the equator

$$\Omega = \Omega_{\text{NS}} \frac{\pi/2 - \theta}{\sqrt{(\pi/2 - \theta)^2 + \Delta\theta^2}}, \quad (\text{B.5})$$

where $\Delta\theta$ was set to 0.1 for all the models. The choice of the effective temperature (set by Q_{NS}) makes some simulations sub-, and the others supersonic. For $\Delta\theta \ll \pi$, subsonic configuration is unstable to Kelvin-Helmholtz instability. Instability at high wavenumbers is suppressed by the finite shear value (Ray 1982), hence the fastest-growing unstable modes are two- and three-armed, with the increment of about Ω_{NS} (see Fig. B.2). The sharper the velocity gradient, the higher the fastest-growing mode. Conservation of angular momentum prevents formation of a single vortex. The primary instability mode changes the overall velocity field into a set of vortices centered in the initial equatorial region. Vorticity evolution during the instability development phase is shown in Fig. B.3.

For the mildly supersonic split-sphere test ($P_{\text{spin}} = 10$ ms), a supersonic shear instability develops on similar timescales close to the rotation period used as the base for the split-sphere rotation. However, instead of vortices, a system of standing shock waves is formed (see Fig. B.4).

As we can see, development of shear instabilities conforms well with the expectations based on analytical and numerical studies of the subject. First, there is dynamical-timescale exponential growth of the instability, subsequently evolving into an equipartition turbulent stage. For the sub-sonic case, numerical resolution does not affect the results considerably during the time span of the calculations.

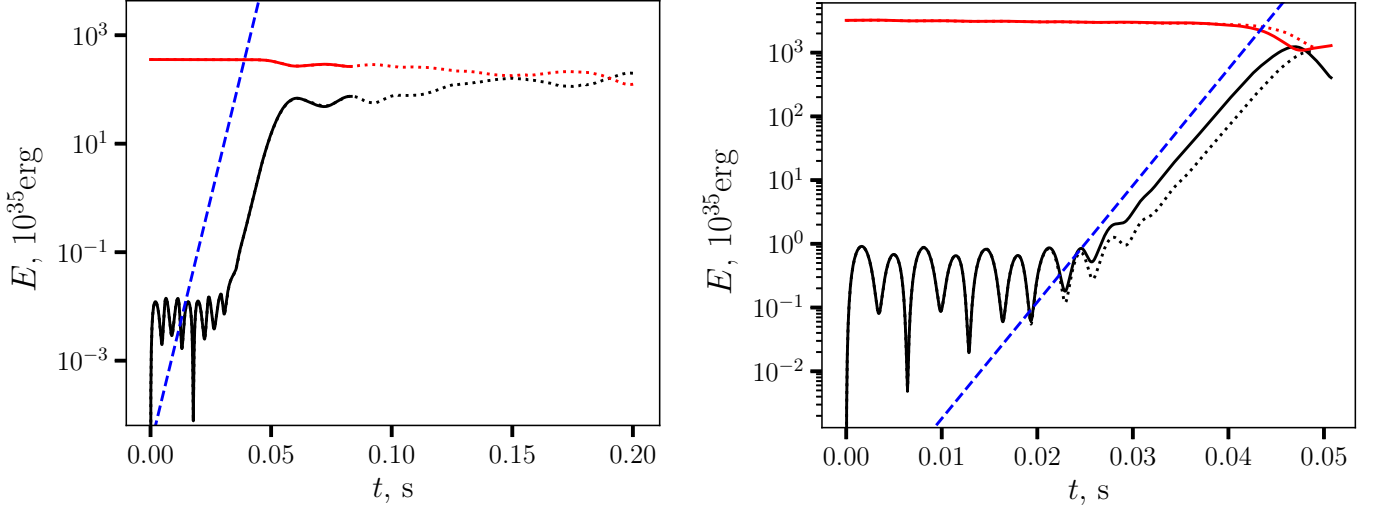


Fig. B.2. Energy evolution and relaxation for the split-sphere test, sub- (left panel) and super-sonic (right panel) cases. Black lines correspond to the part of kinetic energy related to v_θ , red to v_ϕ . Dotted lines are used for lower-resolution models (s)twistLR, solid lines for high-resolution (s)twistHR. Blue dashed lines show an exponential law $\propto e^{\Omega_{\text{NS}} t}$.

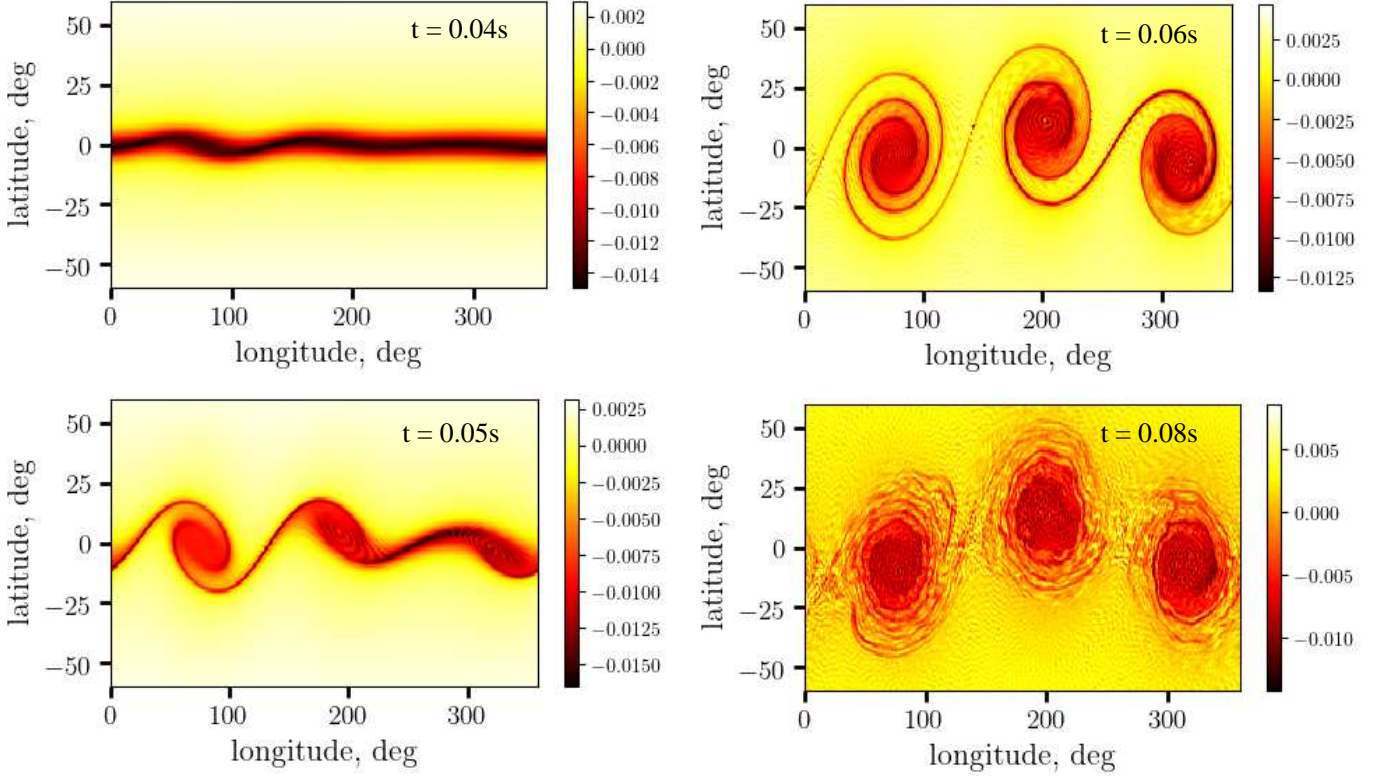


Fig. B.3. Four vorticity snapshots ($t = 0.04, 0.05, 0.06,$ and 0.08s) of the Kelvin-Helmholtz instability development in the split-sphere simulation, model twistHR.

Appendix C: Frequencies of inertial modes on a differentially rotating sphere

Assuming an axisymmetric, differentially rotating velocity background, we linearize the set of dynamic equations and derive a dispersion relation for small-amplitude shallow-water waves on a unit sphere. Perturbed quantities to be considered are density $\rho = \rho_0 + \delta\rho(\theta, \varphi, t)$, longitudinal velocity $v_\varphi = \Omega(\theta) \sin\theta + \delta v_\varphi(\theta, \varphi, t)$, and latitudinal velocity $v_\theta = \delta v_\theta(\theta, \varphi, t)$, where the terms with δ are small perturbations. The background flow is assumed to be pure differential rotation parametrized by angular velocity distribution $\Omega(\theta)$. All the perturbations will be expressed in exponential form $\propto \exp(i(\omega t - k_\theta \theta - k_\varphi \varphi))$.

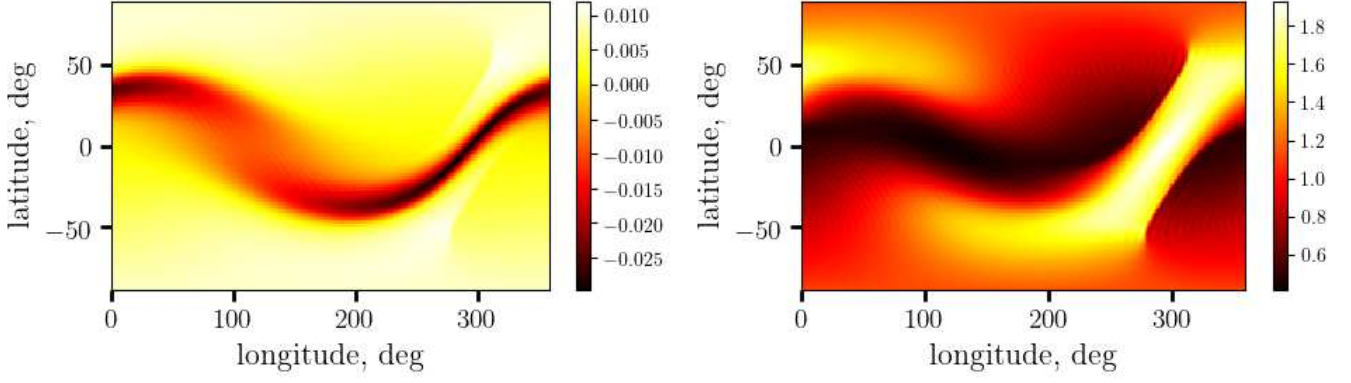


Fig. B.4. A snapshot of the stwistLR simulation at $t = 0.04$ s, when the instability is fully developed and evolves into a system of shock waves. Vorticity is shown on the upper panel, surface density on the lower.

First-order perturbation of the continuity equation in such assumptions is

$$\left(\omega - k_\varphi \Omega\right) \frac{\delta \rho}{\rho} = k_\theta v_\theta + \frac{1}{\sin \theta} k_\varphi \delta v_\varphi. \quad (\text{C.1})$$

The two tangential Euler equations may be in general form written, ignoring the terms containing radial velocities, as

$$\frac{\partial v_\theta}{\partial t} + \frac{v_\varphi}{\sin \theta} \frac{\partial v_\theta}{\partial \varphi} - v_\varphi^2 \cot \theta = -c_s^2 \frac{\partial \ln \rho}{\partial \theta} \quad (\text{C.2})$$

and

$$\frac{\partial v_\varphi}{\partial t} + v_\theta \frac{\partial v_\varphi}{\partial \theta} + \frac{v_\varphi}{\sin \theta} \frac{\partial v_\varphi}{\partial \varphi} + v_\varphi v_\theta \cot \theta = -\frac{c_s^2}{\sin \theta} \frac{\partial \ln \rho}{\partial \varphi}. \quad (\text{C.3})$$

After substituting the expression for the variations of ρ from (C.1), these two equations become, respectively,

$$\left(\tilde{\omega}^2 - c_s^2 k_\theta^2\right) v_\theta = \left(c_s^2 \frac{k_\theta k_\varphi}{\sin \theta} - 2i\Omega \tilde{\omega} \cos \theta\right) \delta v_\varphi, \quad (\text{C.4})$$

and

$$\left(\tilde{\omega}^2 - \frac{c_s^2 k_\varphi^2}{\sin^2 \theta}\right) \delta v_\varphi = \left(c_s^2 k_\theta k_\varphi + i\tilde{\omega} \frac{\partial}{\partial \theta} (\Omega \sin^2 \theta)\right) \frac{v_\theta}{\sin \theta}, \quad (\text{C.5})$$

where $\tilde{\omega} = \omega - k_\varphi \Omega$. Excluding the velocity components v_θ and δv_φ from Eqs. (C.5) and (C.4) yields a dispersion equation

$$\left(\tilde{\omega}^2 - k^2 c_s^2 - \Omega_e^2\right) \tilde{\omega}^2 = ik_\theta k_\varphi c_s^2 \tilde{\omega} \frac{\partial \Omega}{\partial \theta}, \quad (\text{C.6})$$

where

$$k^2 = k_\theta^2 + \frac{k_\varphi^2}{\sin^2 \theta}, \quad (\text{C.7})$$

$$\Omega_e^2 = 2\Omega \cot \theta \frac{\partial}{\partial \theta} (\Omega \sin^2 \theta) \quad (\text{C.8})$$

is the square of the local epicyclic frequency in the sense that a particle with a conserved angular momentum, confined to the surface of the star and being a subject of gravity and centrifugal force, will oscillate in latitudinal direction at this frequency. The possible values of k_φ are restricted by the longitudinal periodic boundary conditions to be $k_\varphi = m$, where m is a whole number.

Two important specific cases may be reproduced when $\omega \gg \Omega$ (sonic waves) and $c_s \rightarrow 0$ (inertial waves):

$$\tilde{\omega}_{\text{sonic}} = \pm c_s k, \quad (\text{C.9})$$

$$\omega_{\text{inertial}} = m\Omega \pm \Omega_e. \quad (\text{C.10})$$

While sonic waves exist only at the frequencies much larger than the spin frequency Ω , inertial modes naturally have frequencies of the same order. Without any loss of generality, we choose the sign in (C.10) to be plus. There is a third set of solutions, present in both limits mentioned above, the entropy modes

$$\omega_{\text{entropy}} = m\Omega. \quad (\text{C.11})$$

In the case of $m = 0$ and $\Omega \simeq \Omega_{\text{NS}}$, the only non-rotating inertial mode has $\omega_{\text{inertial},0} = \Omega_e \simeq 2\Omega \cos \theta$ reproducing the Coriolis oscillation regime. Variability occurring in the regions co-rotating with the NS would produce an equidistant spectrum of eigenmodes

$$\omega_{\text{inertial, co-rotating}} \simeq \Omega_e + m\Omega_{\text{NS}} \quad (\text{C.12})$$

with the frequencies differing by the rotation frequency of the star.